Manipulating Electron Redistribution between Iridium and Co_6Mo_6C Bridging with Carbon Layer Leads to a Significantly Enhanced Overall Water Splitting Performance at Industrial-Level Current Density

Weimo Li,[‡a] Wenqiong Gou,[‡b] Linfeng Zhang,[a] Mengxiao Zhong,[a] Siyu Ren,[a] Guangtao Yu,[b] Ce Wang,[a] Wei Chen,[b]* Xiaofeng Lu[a]*

[a]Alan G. MacDiarmid Institute, College of Chemistry, Jilin University, Changchun 130012, P.R. China. E-mail: xflu@jlu.edu.cn

[b]Engineering Research Center of Industrial Biocatalysis, Fujian Provincial Key Laboratory of Advanced Materials Oriented Chemical Engineering, Fujian-Taiwan Science and Technology Cooperation Base of Biomedical Materials and Tissue Engineering, College of Chemistry and Materials Science, Academy of Carbon Neutrality of Fujian Normal University, Fujian Normal University, Fuzhou 350007, China. E-mail: chenwei@fjnu.edu.cn

‡These authors contributed equally to this work.

†Electronic supplementary information (ESI) available.

Keywords: Ir nanoparticles, Co_6Mo_6C, nitrogen-doped Carbon, industrial-level current density, bifunctional electrocatalyst

1. Experimental section

1.1 Chemicals

Poly(vinylpyrrolidone) (PVP, M_w = 1,300,000 g mol^{-1}) was obtained from Alfa Aesar. Iridium oxide (IrO_2), cobalt nitrate hexahydrate ($Co(NO_3)_2 \cdot 6H_2O$), pyrrole (C_4H_5N), bls(acetylacetonato)dioxomolybdenum(VI) ($C_{10}H_{14}MoO_6$) and sodium dodecyl sulfate (SDS) were acquired from Aladdin Chemistry Co., Ltd. N, N-dimethylformamide (DMF) was purchased from Tianjin Tiantai Chemical Co., Ltd. Iridium chloride hydrate ($IrCl_3 \cdot xH_2O$) and 5 wt% Nafion solution were available from Sigma-Aldrich. Commercial Pt/C (20 wt%) was procured from Johnson Matthey. Ethanol was brought from Sinopharm Chemical Reagent Co. Ltd. Sodium borohydride ($NaBH_4$) was provided by Xilong Chemical Co., Ltd. Iron(III) chloride hexahydrate ($FeCl_3 \cdot 6H_2O$) was received from Tianjin East China Reagent Factory. Ir black was purchased from Heraeus Holding.

1.2 Synthesis of $CoMoO_4$ nanofibers

Initially, a typical electrospinning technique was carried out to fabricate precursor nanofibrous membrane. Specifically, 0.2326 g of $Co(NO_3)_2 \cdot 6H_2O$, 0.2609 g of $C_{10}H_{14}MoO_6$ and 0.5 g of PVP were dissolved in the mixture solution comprising 3 mL of DMF and 3 mL of ethanol under continuous stirring until it became a homogenous solution. The prepared electrospun precursor solution was then sealed into a syringe with the propulsion rate of 0.02 mm min^{-1} and the tip of its needle is 20 cm far away from the aluminum foil collector. Under the high voltage of 16 kV, precursor nanofibrous membrane was fabricated. Subsequently, a calcination procedure was performed and the above prepared membrane was conveyed into the muffle furnace under an air atmosphere at 150 °C for 1 h with a heating speed of 1 °C min^{-1}, followed by 550 °C for 2 h with a heating speed of 2 °C min^{-1}. The final product was $CoMoO_4$ nanofibers ($CoMoO_4$ NFs).

1.3 Synthesis of $CoMoO_4$-PPy nanofibers

The formation of $CoMoO_4$-PPy nanofibers ($CoMoO_4$-PPy NFs) was accomplished via an in situ polymerization process. 5 mg of $CoMoO_4$ NFs were dispersed into 15 mL

of water under vigorous stirring. Subsequently, 70 μL of pyrrole and 1 mg of SDS were added into the above dispersion and stirred for 1 h. The solution was subjected to refrigeration for a modest duration of 5 min prior to the introduction of 10 mL of $FeCl_3$ solution (7 mg mL^{-1}) within the solution. Following a rigorous in situ polymerization procedure with a continuous stirring for 2 h, the resultant $CoMoO_4$-PPy NFs were thoroughly washed with water for several times and finally freeze-dried in vacuum overnight. Moreover, $CoMoO_4$ NFs with varied contents of PPy was accomplished by adding diverse contents of pyrrole and $FeCl_3$. The $CoMoO_4$-50PPy NFs and $CoMoO_4$-90PPy NFs are synthesized by adding 50 and 90 μL of pyrrole and 10 mL of $FeCl_3$ (5 and 9 mg mL^{-1}), respectively, alongside other procedure steps remaining unchanged.

1.4 Synthesis of Co_6Mo_6C-Ir nanofibers

$CoMoO_4$-PPy NFs were firstly put into a tubular furnace and subjected to a calcination process under an Ar atmosphere at 800 °C for 3 h with a heating speed of 2 °C min^{-1}. After that, the Co_6Mo_6C nanofibers (Co_6Mo_6C NFs) were obtained. In the following, 4 mg of Co_6Mo_6C NFs and a certain amount of $IrCl_3$ solution (10 mg mL^{-1}) were added into 10 mL of water with a vigorous shaking on the rotary shaker for 45 min, followed by the addition of 200 μL of $NaBH_4$ solution (10 mg mL^{-1}). At last, the obtained Co_6Mo_6C-Ir NFs were rinsed with water for several times and freeze-dried in vacuum overnight. The volume additions of $IrCl_3$ solution in the dispersion of Co_6Mo_6C NFs are 70, 100 and 130 μL (denoted as Co_6Mo_6C-Ir-1 NFs, Co_6Mo_6C-Ir-2 NFs and Co_6Mo_6C-Ir-3 NFs, respectively). Moreover, $CoMoO_4$-50PPy NFs and $CoMoO_4$-90PPy NFs were also calcined at 800 °C for 3 h and then react with 100 μL of $IrCl_3$ (10 mg mL^{-1}) in the presence of $NaBH_4$, which are denoted as $CoMoO_4$-50PPy-800 NFs, $CoMoO_4$-90PPy-800 NFs, $CoMoO_4$-50PPy-800-Ir-2 NFs and $CoMoO_4$-90PPy-800-Ir-2 NFs, respectively.

1.5 Characterizations

The morphology details pertaining to the as-synthesized catalysts were characterized by field-emission scanning emission microscopy (FESEM, FEI Nova NanoSEM) and transmission electron microscopy (TEM, JEOL JEM-2100), respectively. The associated elemental composition distributions and crystalline

structures were confirmed via the high-angle annular dark-field scanning transmission electron microscopy (HAADF-STEM) image, elemental mapping analysis, energy-dispersive X-ray (EDX) patterns and high-resolution TEM (HRTEM) images, which were accomplished by FEI Tecnai G2 F20. An inductively coupled plasma (ICP, Agilent 725) was employed to quantify each element content in the synthesized catalysts. X-ray diffraction (XRD, PANalytical B.V. Empyrean with Cu Kα radiation), Raman profiling (LabRAM HR Evolution) and X-ray photoelectron spectroscopy (XPS, Thermo Fisher Scientific ESCALAB 250) were employed to further probe the valence states and atomic arrangement of the as-synthesized catalysts.

1.6 Electrochemical measurements

All the electrochemical measurements were executed on the CHI660E electrochemical workstation under alkaline environment at ambient temperature. The evaluations of HER and OER performance tests were accomplished through a three-electrode configuration in 1 M KOH solution. During the electrochemical tests, catalyst-loaded carbon paper (CP), Hg/HgO electrode as along with Pt wire (for OER test) or graphite rod (for HER test) are utilized as the working electrode, reference electrode and counter electrode, respectively. In the preparation procedure of working electrode, 4 mg of catalyst is blended with 990 μL of water, 990 μL of ethanol and 20 μL of 5 wt% Nafion solution and then conducts a continuous ultrasonication. Next, 50 μL of the prepared catalyst ink is dropped on the surface of CP (0.09 cm^2) to achieve the modified working electrode. Furthermore, to obtain precise electrochemical data, the calibration of Hg/HgO electrode toward reversible hydrogen electrode (RHE) in alkaline environment is also conducted (Fig. S48).

Prior to the acquisition of electrochemical data, several cyclic voltammetry (CV) cycles were executed in an Ar-saturated 1 M KOH solution to attain a steady state throughout the system. During the electrochemical tests, for the precise electrochemical data, linear scan voltammetry (LSV) was implemented with a scan rate of 1 mV s^{-1}. Electrochemical impedance spectroscopy (EIS) was executed at a frequency domain of 0.1-10^5 Hz and executed at -1.2 and 0.68 V *vs.* Hg/HgO electrode for HER and OER process, respectively. The double-layer capacitance (C_{dl}) was acquired via CV

measurements with various scan rates (10, 20, 30, 40, 50, 60, 70, 80, 90, 100 mV s^{-1}) within the potential domains of -0.3 to -0.2 V *vs.* Hg/HgO electrode. The electrochemical active surface area (ECSA) is also calculated, which is linearly proportional to the C_{dl}. The corresponding formula is illustrated below:

$$ECSA = C_{dl}/C_s$$

Roughness factor (RF) is also calculated below:

$$RF = ECSA/S$$

The mass activity with regard to noble metal (MA_{NM}) is calculated below:

$$\text{Mass activity (MA)} = j \times S/m_{NM}$$

Turnover frequency (TOF) values is calculated below:

$$TOF = j \times S/(z \times F \times n_{metal})$$

where C_s denotes the specific capacitance for a 1 cm^2 flat surface, which is predominantly recognized as 0.04 mF cm^{-2} in alkaline solution; S signifies the surface area covered by catalysts; j depicts the current density; m_{NM} signifies the mass of noble metal; z refers to the accepted or donated electrons for the generation of each H_2 or O_2 molecule (2 for HER process and 4 for OER process); F signifies the Faraday constant (96485.3 C mol^{-1}); n_{metal} denotes the quantity of moles of all the active metal (the lowest TOF values are calculated). All aforementioned electrochemical data were collected with iR compensation.

A two-electrode system was employed to assess the OWS performance of the assembled alkaline electrolyzers. The LSV curves were performed at 1 mV s^{-1}. The Faraday efficiencies (FEs) of the electrolyzers were measured by collecting gas through drainage method at the current density of 200 mA cm^{-2}.

The FE is calculated as follows:

$$FE = [z \times F \times n_{gas}/(I \times t)] \times 100\%$$

$$n_{gas} = V_{gas}/V_m$$

z denotes the captured or donated electrons for the generation of each H_2 or O_2 molecule (2 for HER process and 4 for OER process); F signifies the Faraday constant (96485.3 C mol^{-1}); n_{gas} represents the quantity of moles of gas evolved; I symbolizes the constant current applied for t min; V_m denotes molar volume of gas (24.5 L mol^{-1} at room

temperature). All the OWS electrochemical examinations were conducted with the CP as the substrate, except for the durability test (nickel foam was chosen as the substrate).

2. Theothetical section

2.1 Computational methods

Under the density functional theory (DFT), all computations are performed within the rigorous framework of the Vienna *ab initio* simulation package (VASP) [1]. The exploitation of exchange correlation energy is informed by the generalized gradient approximation (GGA) fortified with the Perdew-Burke-Enzzerhof (PBE) formulation [2], wherein the semi-empirical van der Waals (vdW) methodology (DFT-D2) devised by Grimme is incorporated to encompass the dispersion interaction [3,4]. The utilization of projector-augmented plane wave (PAW) serves to simulate the electron-ion interactions [5], and a 450-eV energy cutoff is applied for the plane-wave basis set. Three different configurations of 3×3×3, 3×3×1 and 2×3×1 Monkhorst-Pack grid k-points are employed respectively for the geometric optimization of the bulk structure and the corresponding slab model of Co_6Mo_6C, as well as the intricate assembly composed of the ultra-thin carbon layer overlying the Co_6Mo_6C. The convergence threshold is set as 10^{-4} eV in energy. For all simulations of the slab models, the symmetrization was switched off and the dipolar correction was included.

2.2 Theoretical models

The bulk Co_6Mo_6C possesses a cubic structure and is classified into the space group $Fd\bar{3}m$ (Fig. S33a online). The optimized lattice parameter a is approximately 10.772 Å, which conforms nicely to the corresponding experimental value (10.897 Å). By disassembling the optimized bulk Co_6Mo_6C framework through the low-index (100) plane, we obtained two different surfaces terminated by Co- and MoC-layers, as shown in Figs. S33b and S33c (online). Each configuration can be simulated with the corresponding slab model comprising five stoichiometric Co_6Mo_6C layers. Within the theoretical models, the upper two layers are relaxed devoid of any symmetry or direction restrictions, while the underlying layers remain fixed throughout the

computational process. Based on the aforementioned models, the corresponding surface energies (γ) are estimated by the equation below, which was used to quantify the excess energy of the surface with respect to the bulk [6].

$$\gamma = \frac{E_{slab} - nE_{bulk}}{A} - \frac{E_{slab}^{unrelax} - nE_{bulk}}{2A}$$

where E_{slab} is the total energy of the slab (relaxed on one side), $E_{unrelax}$ is the total energy of the unrelaxed slab, n is the number of Co_6Mo_6C units in the slab structure. Moreover, E_{bulk} is the energy of a Co_6Mo_6C formula unit in bulk structure, and A is the surface area of one side of the slab. Our results verify that the calculated surface energies are 0.220 and 0.231 J/m^2 for the Co-terminated and MoC-terminated slabs, respectively, implying that the configuration of Co-termination is more stable in terms of energy. It will be selected as the structural unit for constructing the theoretical model of subsequent composite system.

Specifically, based on the relevant experimental data, we formulated the corresponding theoretical model of Co_6Mo_6C-Ir NFs system by enveloping the N-doped graphene on the Co-terminated Co_6Mo_6C slab, to simulate the ultra-thin N-doped carbon layer enveloping the Co_6Mo_6C system. The lattice mismatch between them is noted to be be almost negligible (within 4%). Within this theoretical model, two distinct types of nitrogen atoms (*i.e.*, pyridine nitrogen and graphitic nitrogen) are introduced into the N-doped graphene, considering the circumstance that they can be predominantly observed in our experiment. Subsequently, the Ir_4 structure representing the Ir metal cluster is deposited on the surface of N-doped graphene covering Co_6Mo_6C system. Our computational findings disclose that the Ir_4 cluster can be stably anchored on the material surface, and the three representative Ir atoms at the bottom are connected by carbon, pyridine nitrogen or carbon atoms adjacent to graphitic nitrogen, respectively. Throughout the computations, the bottom layer comprising stoichiometric Co_6Mo_6 C units is frozen, while the rest are completely relaxed.

2.3 The free-energy calculations on hydrogen evolution reaction (HER)

The HER catalytic activity can be assessed by determining the adsorption free

energy of H* (ΔG_{H^*}). The ΔG_{H^*} value can be calculated via the equation $\Delta G_{H^*} = \Delta E_{H^*} + \Delta E_{ZPE} - T\Delta S$, where ΔE_{H^*}, ΔE_{ZPE} and ΔS represent the binding energy, zero point energy change and entropy change of H* adsorption, respectively. Among them, ΔE_{H^*} can be obtained through the formula $\Delta E_{H^*} = E_{slab\text{-}H} - E_{slab} - 1/2\ E_{H2}$, wherein E_{H2} denotes the total energy of an individual H_2 molecule, and $E_{slab\text{-}H}/E_{slab}$ is the total energy of the slab model with/without H*. Furthermore, due to the negligible vibrational entropy of H*, we can compute ΔS via the relationship $\Delta S = S_{H^*} - 1/2S_{H2} \approx -1/2S_{H2}$. Hence, the $T\Delta S$ value can be -0.205 eV, given that TS_{H2} is 0.41 eV for H_2 at 300 K and 1.0 atm. Additionally, we can ascertain ΔE_{ZPE} for H* through the formula $\Delta E_{ZPE} = E_{ZPE}(H^*) - 1/2E_{ZPE}(H_2)$. Our calculated $\Delta E_{ZPE}(H_2)$ value is approximately 0.305 eV, which aligns closely with the reported result by Norskov *et al* [7].

2.4 The free-energy calculations on oxygen evolution reaction (OER)

The OER reaction is one of the half reactions in water splitting process, which usually consists of four fundamental reaction steps, as shown in the following formulas (1)-(4):

$$H_2O + * \rightarrow OH^* + H^* + e^- \quad (1)$$

$$OH^* \rightarrow O^* + H^+ + e^- \quad (2)$$

$$H_2O + O^* \rightarrow OOH^* + H^+ + e^- \quad (3)$$

$$OOH^* \rightarrow O_2 + * + H^+ + e^- \quad (4)$$

where * means an active site on the catalyst surface, and OH*, O* or OOH* represent three different intermediates.

In accordance with the structural model of composite system, the computational hydrogen electrode (CHE) model proposed by Nørskov *et al*. is utilized to assess the reaction Gibbs free energy change (ΔG) [8,9], and the ΔG value for each step of OER is defined as:

$$\Delta G = \Delta E + \Delta E_{ZPE} - T\Delta S + \Delta G_U + \Delta G_{pH}$$

where ΔE, ΔE_{ZPE} and ΔS signify the change of total energy, the change of zero-point energy and entropy prior and subsequent to the reaction, respectively, and T signifies the reaction temperature. The influence of the applied external electrode potential (U)

is ΔG_U=-ne$U$, where n signifies the number of electrons transferred during the reaction. ΔG_{PH}=-k_BTln10×pH contributes a correction for free energy reliant on the concentration of H^+ ions, wherein k_B denotes the Boltzmann constant, and pH is considered as zero for an acidic medium. Regarding the steps involving proton-electron pair transfer, the free energy $G(H^+ + e^-)$ is approximately equal to $1/2G(H_2)$. The Gibbs free energy value for oxygen is attained from the equation $G_{O2} = 2G_{H2O} - 2G_{H2} + 4.92$ eV [10]. The overpotential (η) value of OER can be estimated by using the following formula:

$$\eta = \max \{\Delta G_a, \Delta G_b, \Delta G_c, \Delta G_d\}/e - 1.23 \text{ V}$$

As is well establised, η is frequently employed to assess the catalytic activity of oxygen evolution catalysts. The smaller η, the higher the OER catalytic activity. In the case where pH = 0, based on the Nernst equation, the equilibrium electrode potential is 1.23 V.

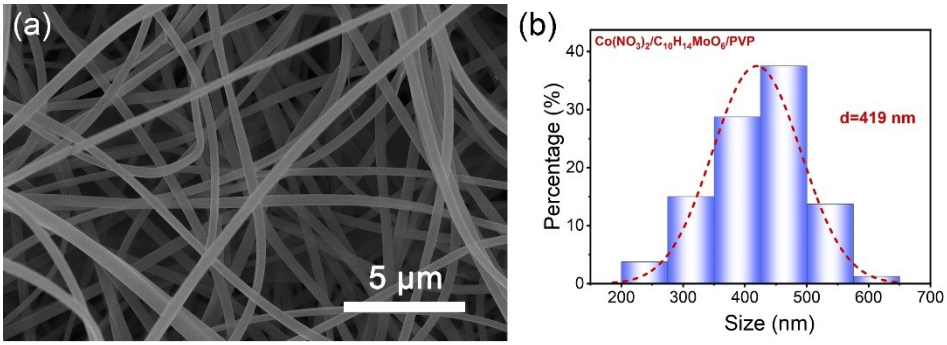

Figure S1. (a) SEM image and (b) diameter distribution of precursor nanofibers.

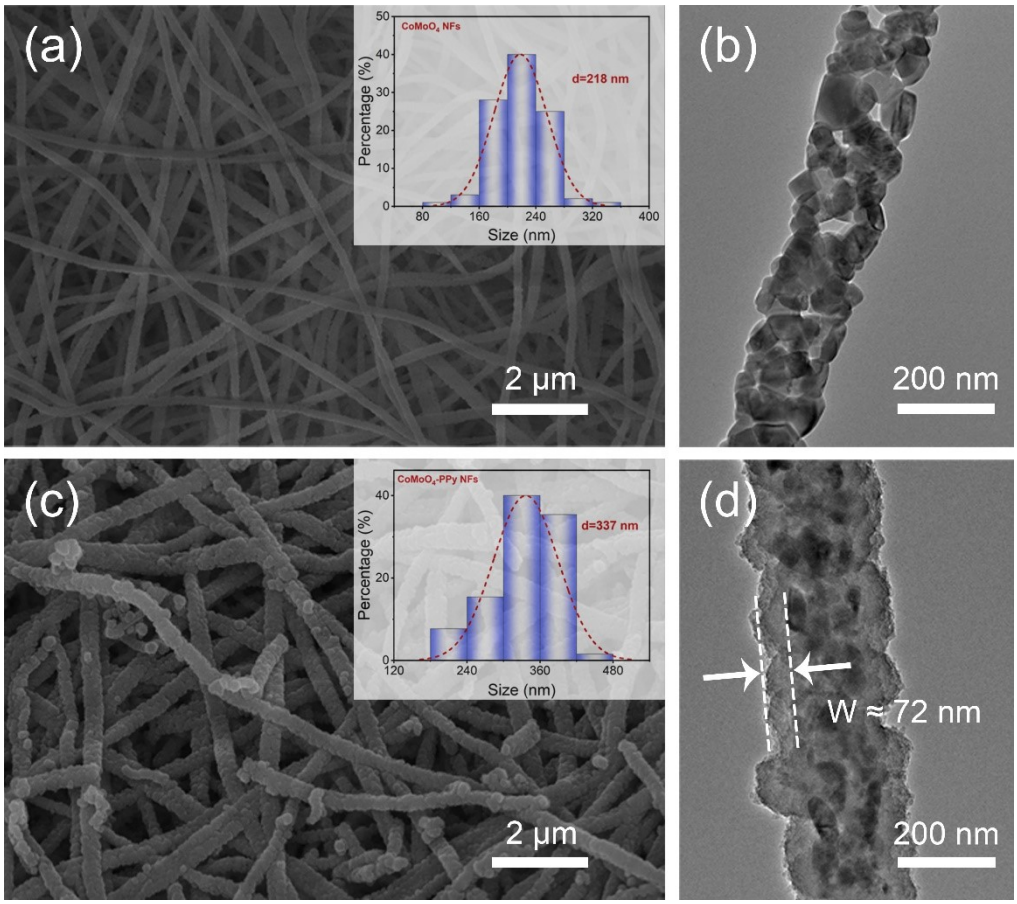

Figure S2. (a, c) SEM and (b, d) TEM images of (a, b) $CoMoO_4$ NFs and (c, d) $CoMoO_4$-PPy NFs. Insets of (a, c): Diameter distributions of $CoMoO_4$ NFs and $CoMoO_4$-PPy NFs.

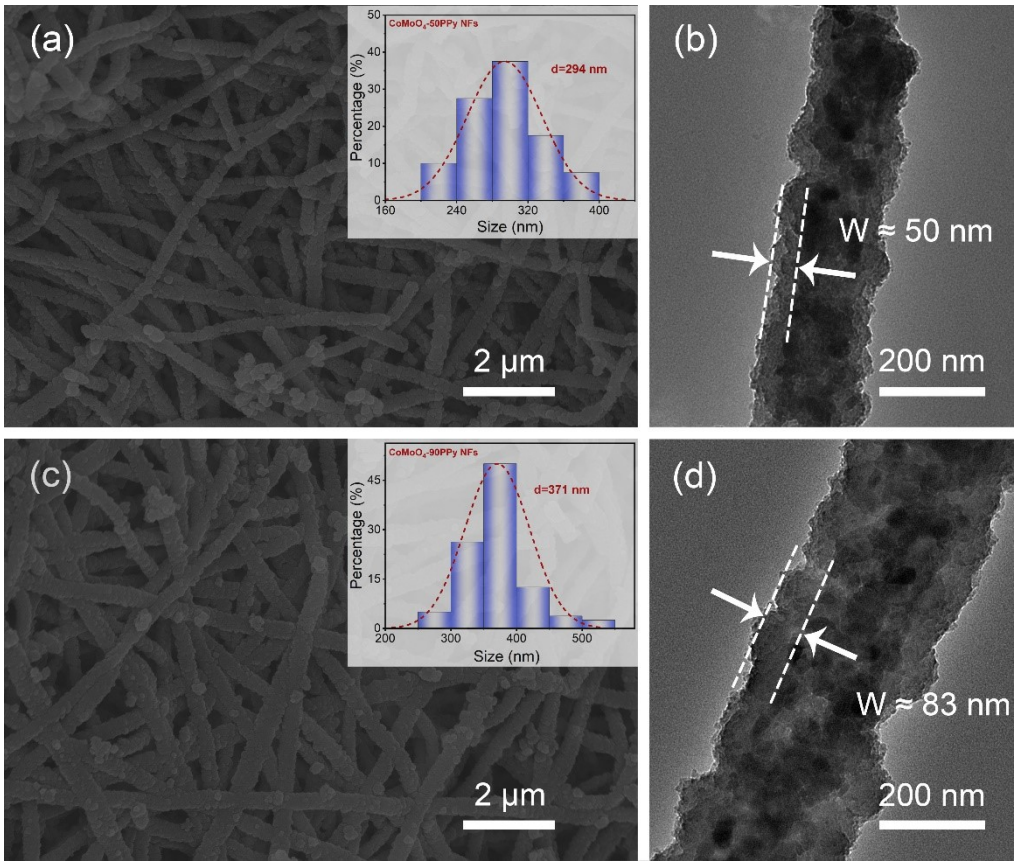

Figure S3. (a, c) SEM and (b, d) TEM images of (a, b) $CoMoO_4$-50PPy NFs and (c, d) $CoMoO_4$-90PPy NFs. Insets of (a, c): Diameter distributions of $CoMoO_4$-50PPy NFs and $CoMoO_4$-90PPy NFs.

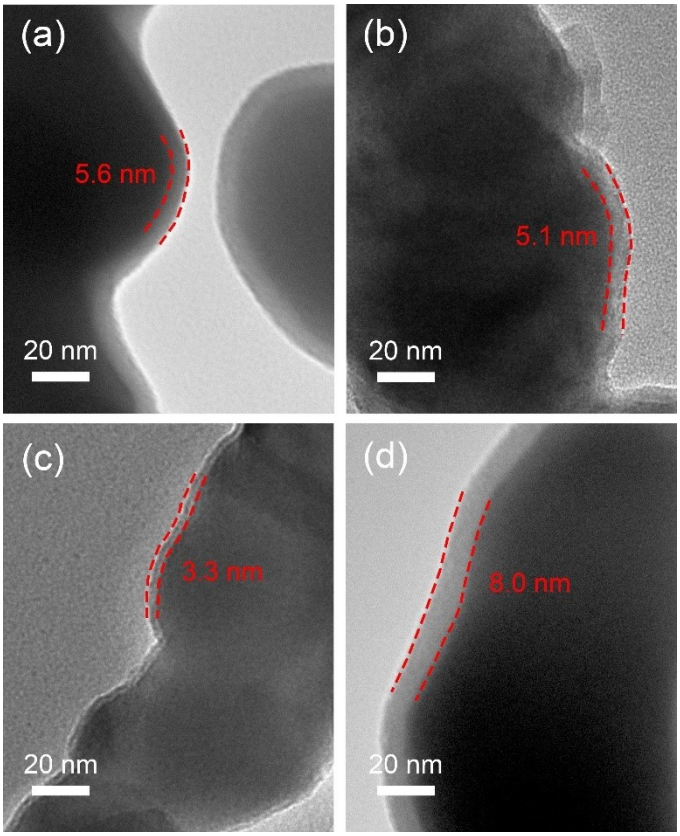

Figure S4. (a-d) TEM images to show the thickness of carbon layer of Co_6Mo_6C-Ir-2 NFs for different preparation batches.

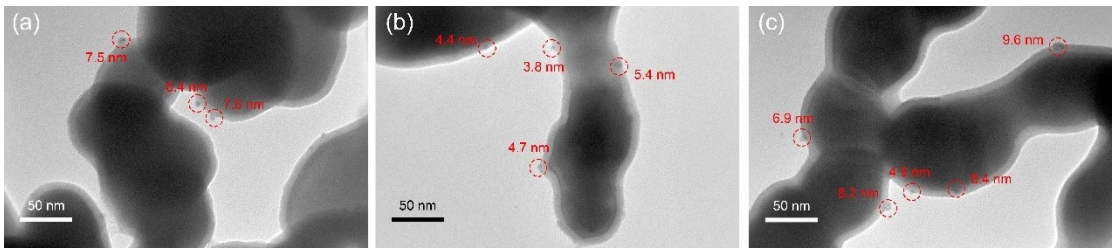

Figure S5. (a-c) The enlarge TEM images of Co_6Mo_6C-Ir-2 NFs.

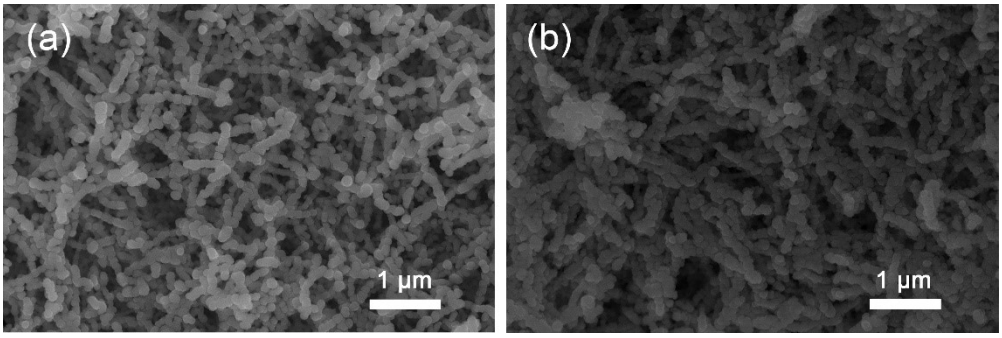

Figure S6. SEM images of (a) Co_6Mo_6C-Ir-1 NFs and (b) Co_6Mo_6C-Ir-3 NFs.

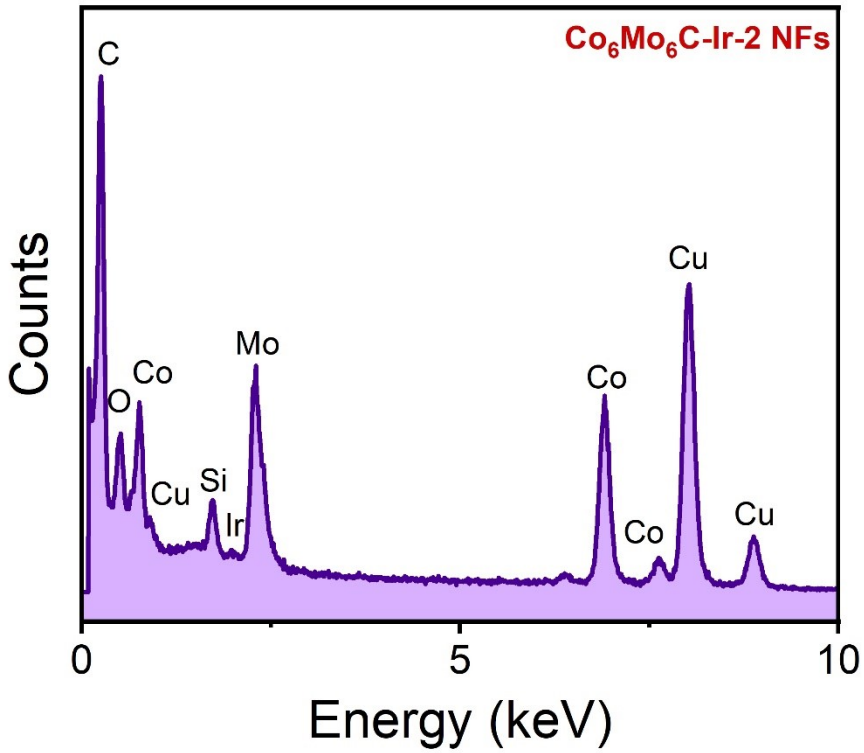

Figure S7. EDX spectrum of Co_6Mo_6C-Ir-2 NFs.

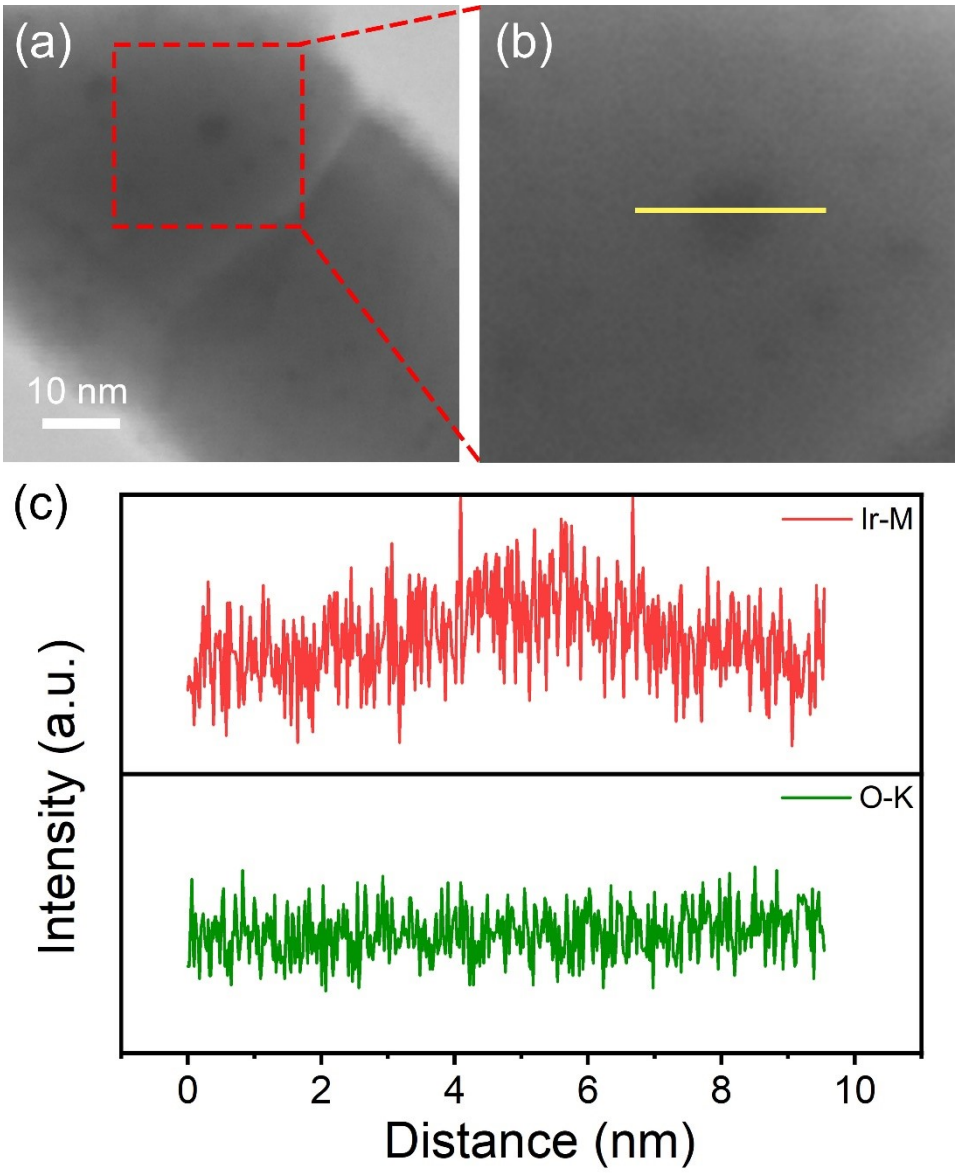

Figure S8. (a) STEM image, (b) enlarged STEM image and (c) HADDF/STEM line scans of Co_6Mo_6C-Ir-2 NFs.

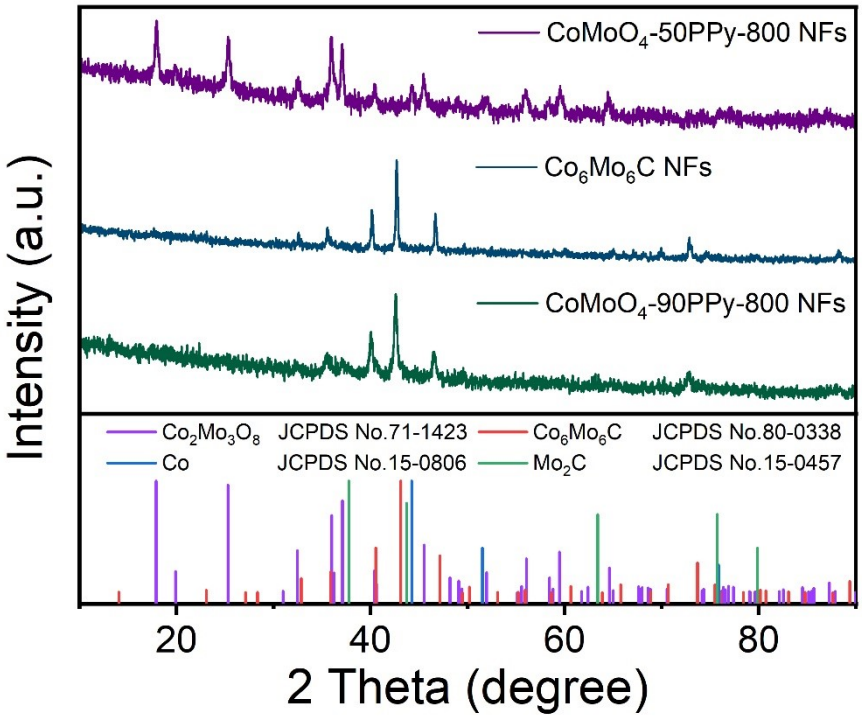

Figure S9. XRD patterns of $CoMoO_4$-50PPy-800 NFs, Co_6Mo_6C NFs and $CoMoO_4$-90PPy-800 NFs.

Note: The $CoMoO_4$-50PPy-800 NFs show the diffraction peaks that correspond to $Co_2Mo_3O_8$ (JCPDS No. 71-1423) and Co (JCPDS No. 15-0806), while the diffraction peaks of $CoMoO_4$-90PPy-800 NFs are ascribed to Co_6Mo_6C (JCPDS No. 80-0338) and Mo_2C (JCPDS No. 15-0457).

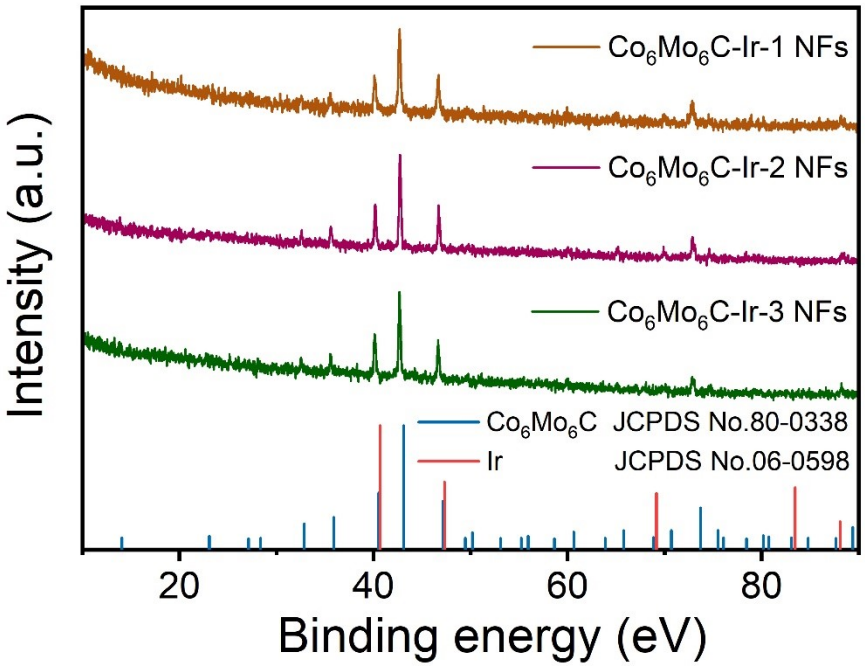

Figure S10. XRD patterns of Co_6Mo_6C-Ir-1 NFs, Co_6Mo_6C-Ir-2 NFs and Co_6Mo_6C-Ir-3 NFs.

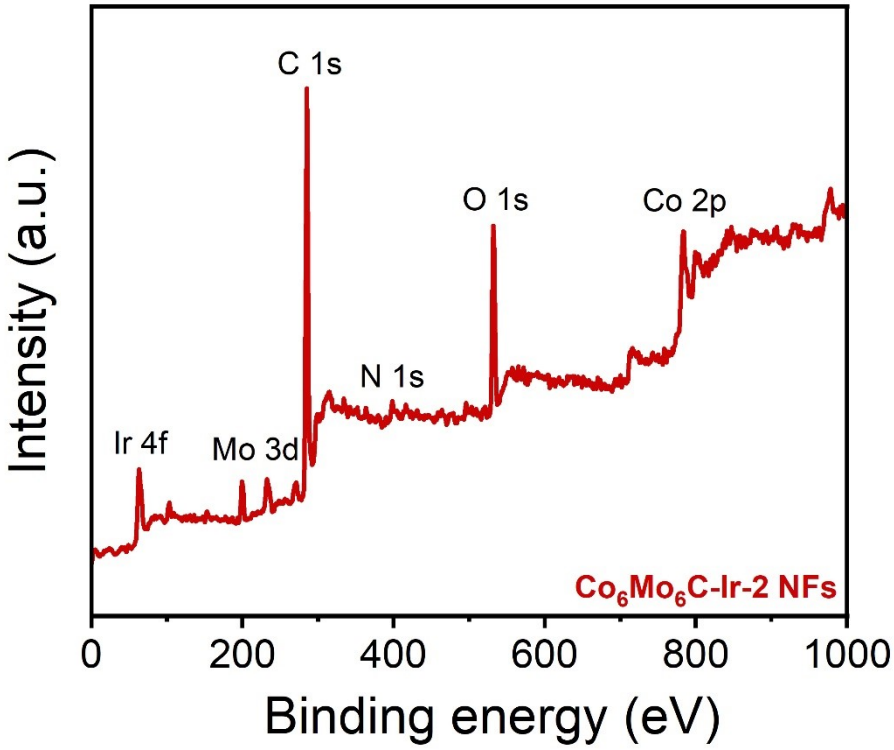

Figure S11. The XPS survey spectrum of Co_6Mo_6C-Ir-2 NFs.

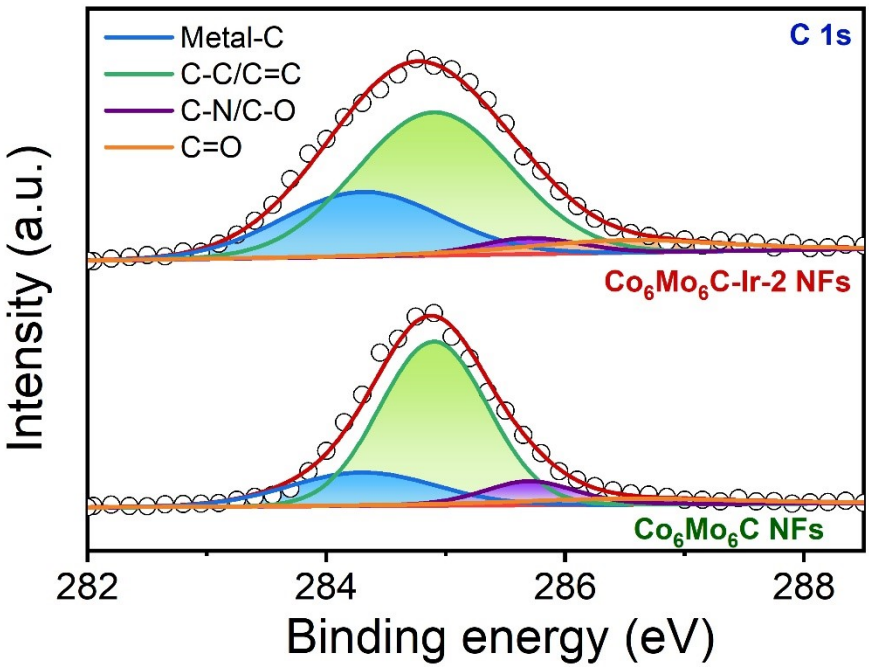

Figure S12. Typical high-resolution C 1s XPS spectra of Co_6Mo_6C NFs and Co_6Mo_6C-Ir-2 NFs.

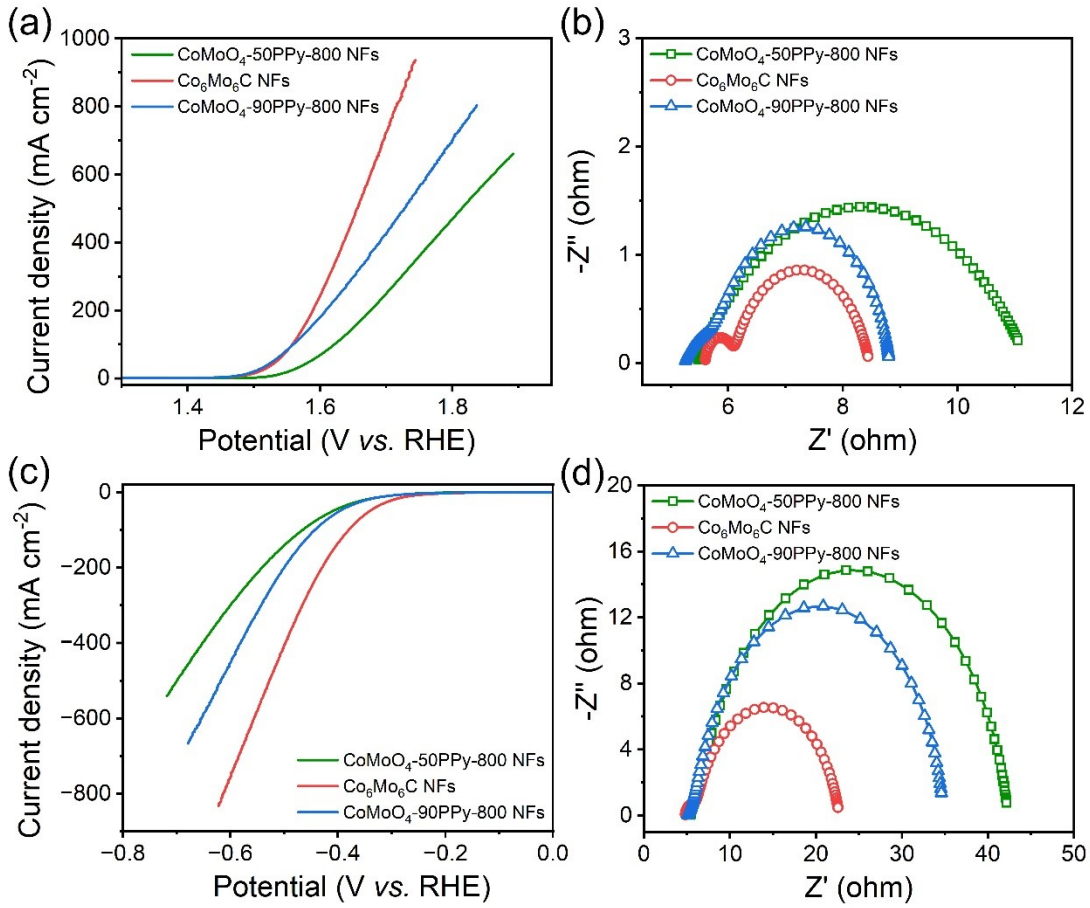

Figure S13. (a, c) LSV curves and (b, d) Nyquist plots of Co_6Mo_6C NFs and other catalysts for OER and HER.

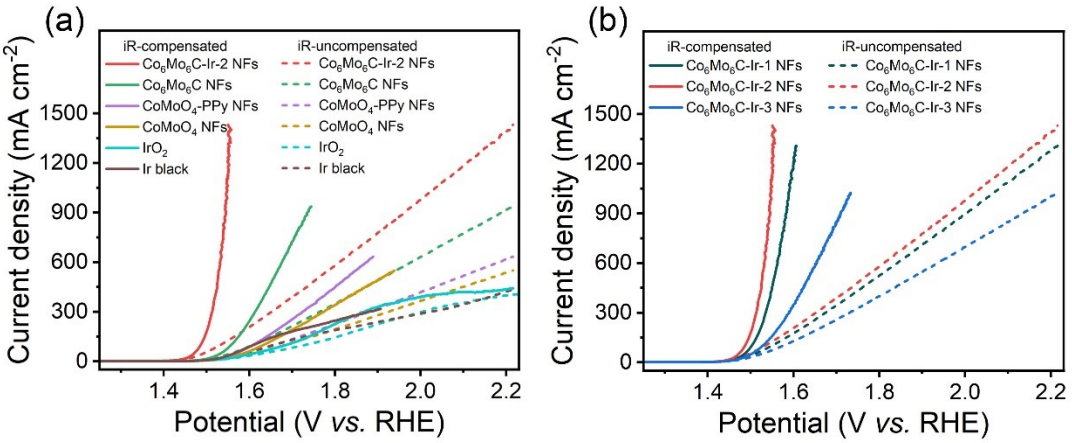

Figure S14. (a, b) The LSV curves of varied catalysts with and without iR compensation for OER.

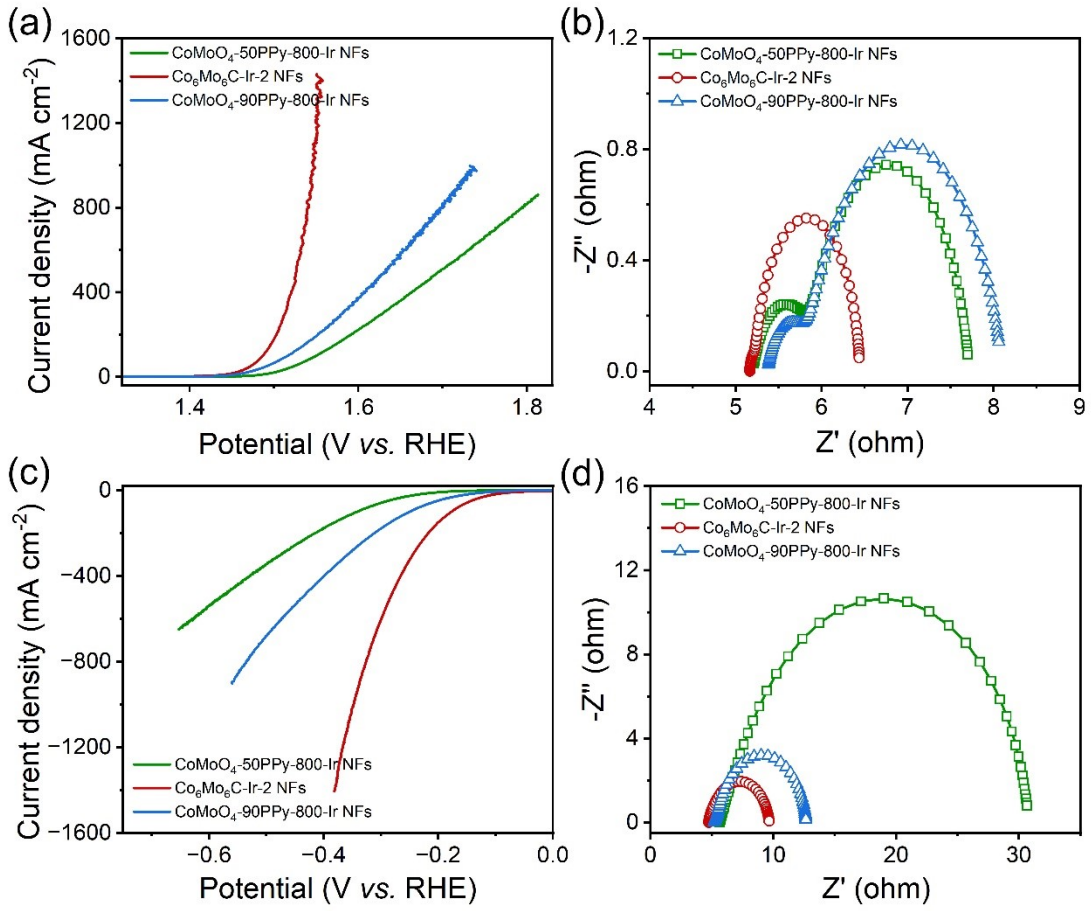

Figure S15. (a, c) LSV curves and (b, d) Nyquist plots of Co_6Mo_6C-Ir-2 NFs and other catalysts for OER and HER.

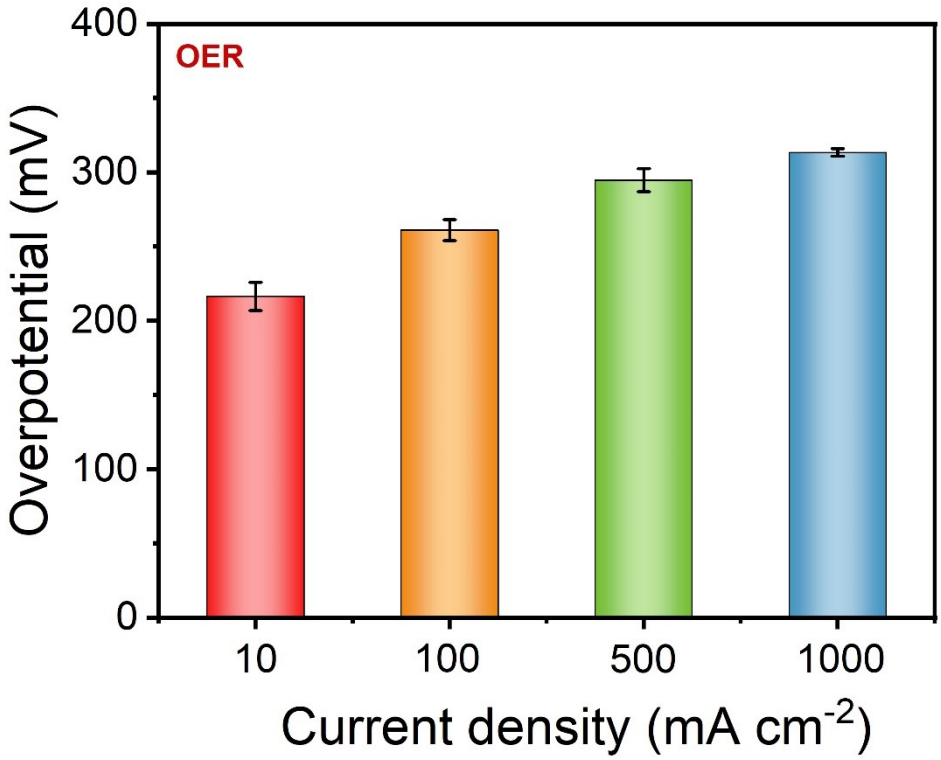

Figure S16. The evaluation of the OER overpotentials of Co_6Mo_6C-Ir NFs at 10, 100, 500 and 1000 mA cm^{-2}. Error bars represent the standard deviations of three independent measurements under the same conditions.

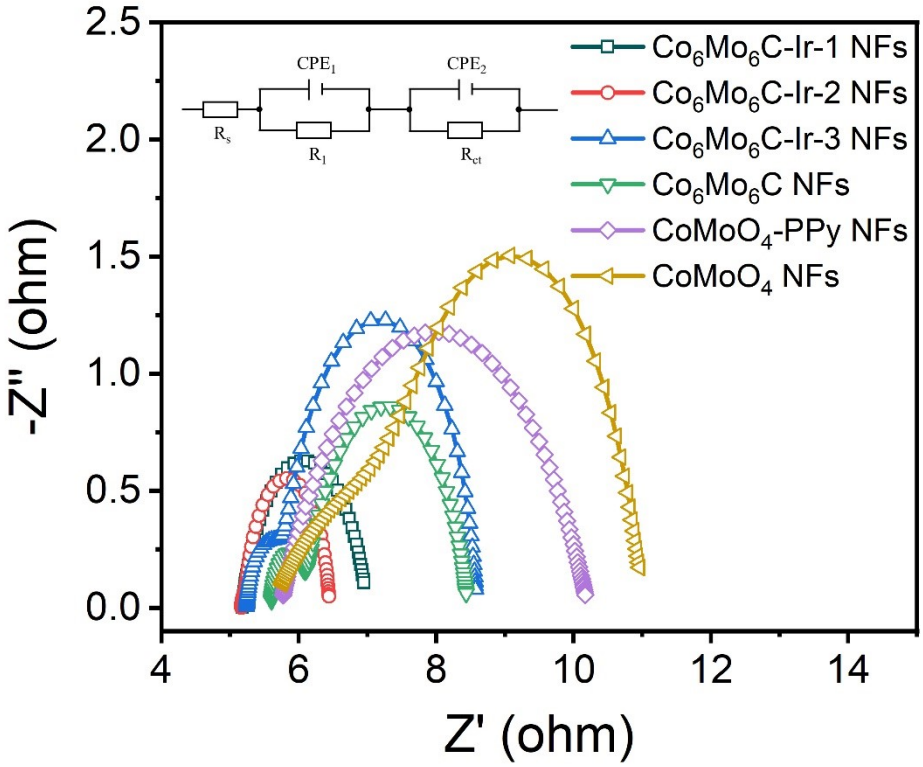

Figure S17. Nyquist plots of Co_6Mo_6C-Ir-2 NFs and other catalysts that performed at 0.68 V *vs.* Hg/HgO electrode.

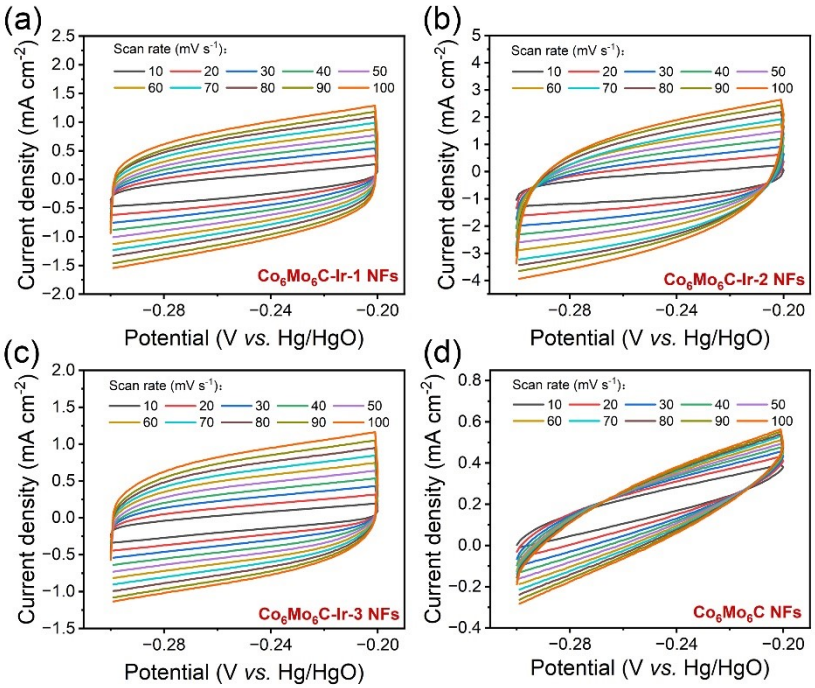

Figure S18. The CV curves of (a) Co_6Mo_6C-Ir-1 NFs, (b) Co_6Mo_6C-Ir-2 NFs, (c) Co_6Mo_6C-Ir-3 NFs and (d) Co_6Mo_6C NFs with different scan rates from 10 to 100 mV s^{-1}.

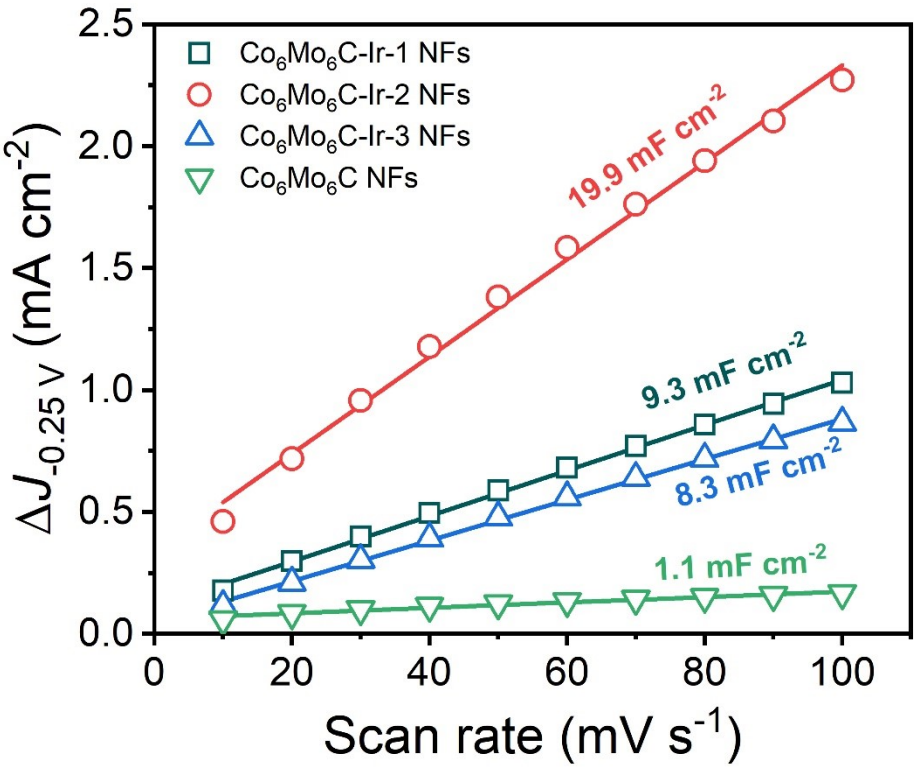

Figure S19. C_{dl} values obtained from the linear fitting of capacitance currents and scan rates.

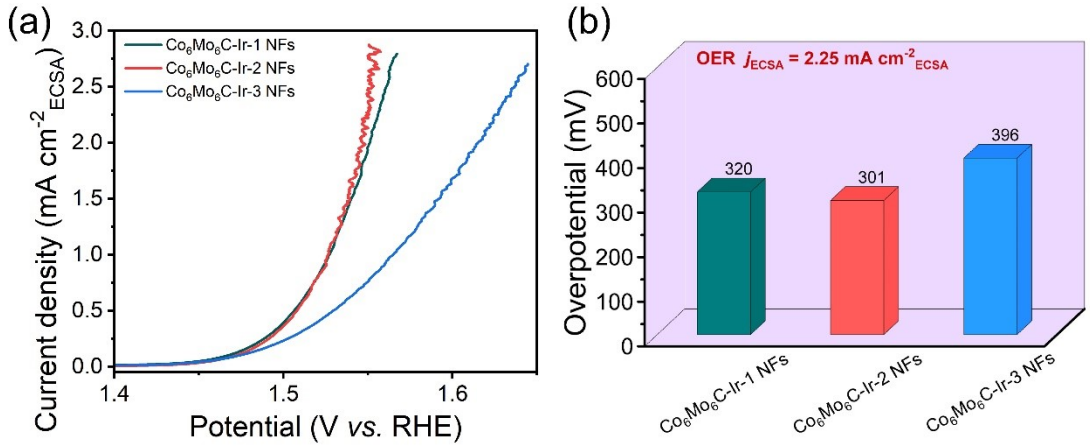

Figure S20. (a) OER polarization curves normalized to ECSA in 1 M KOH. (b) The corresponding specific activities at the current density of 2.25 mA cm^{-2}_{ECSA}.

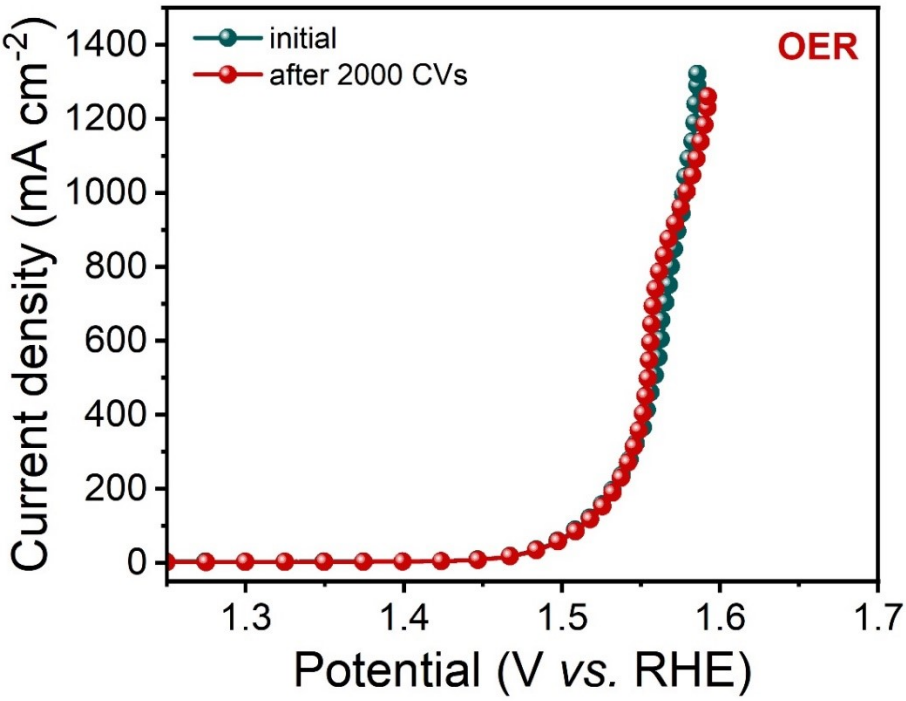

Figure S21. The LSV curves of Co_6Mo_6C-Ir-2 NFs for OER before and after 2000 CVs.

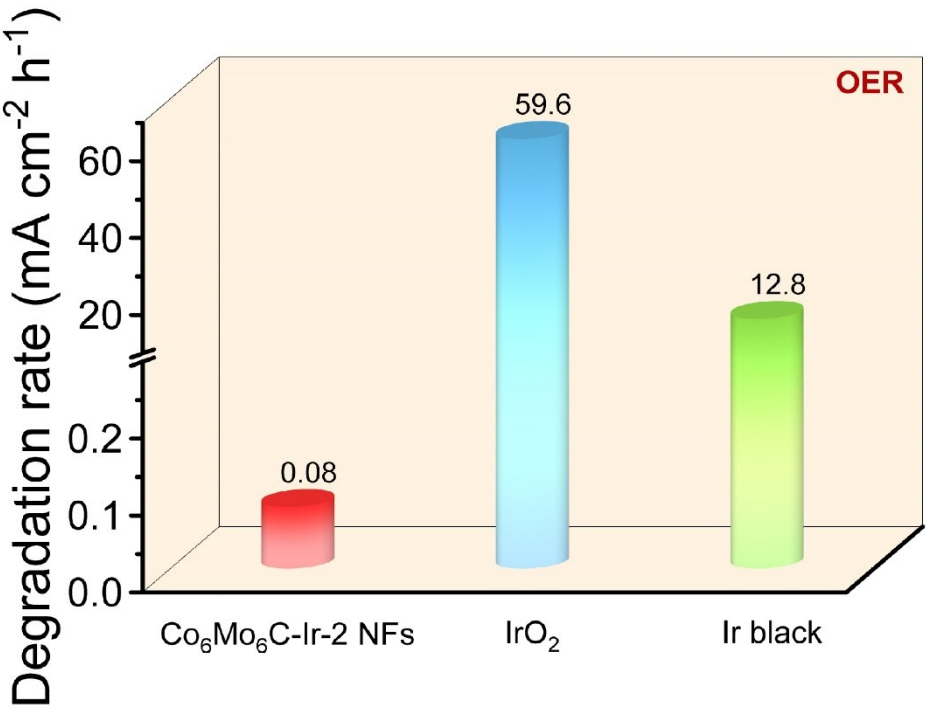

Figure S22. The degradation rates of catalysts for OER stability test.

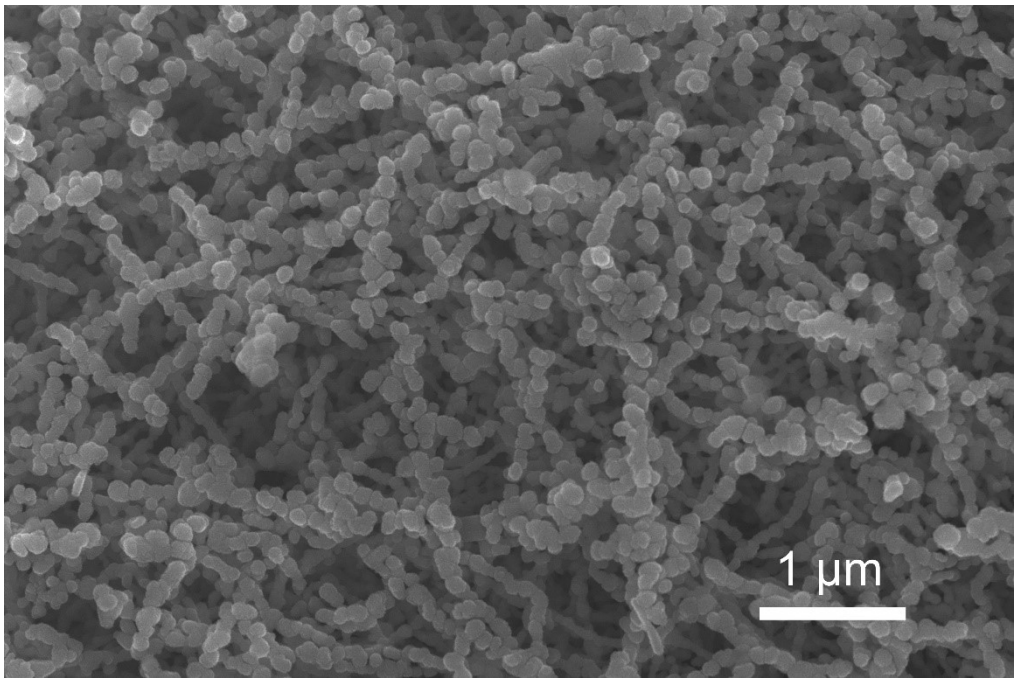

Figure S23. The SEM image of Co_6Mo_6C-Ir-2 NFs after OER stability test.

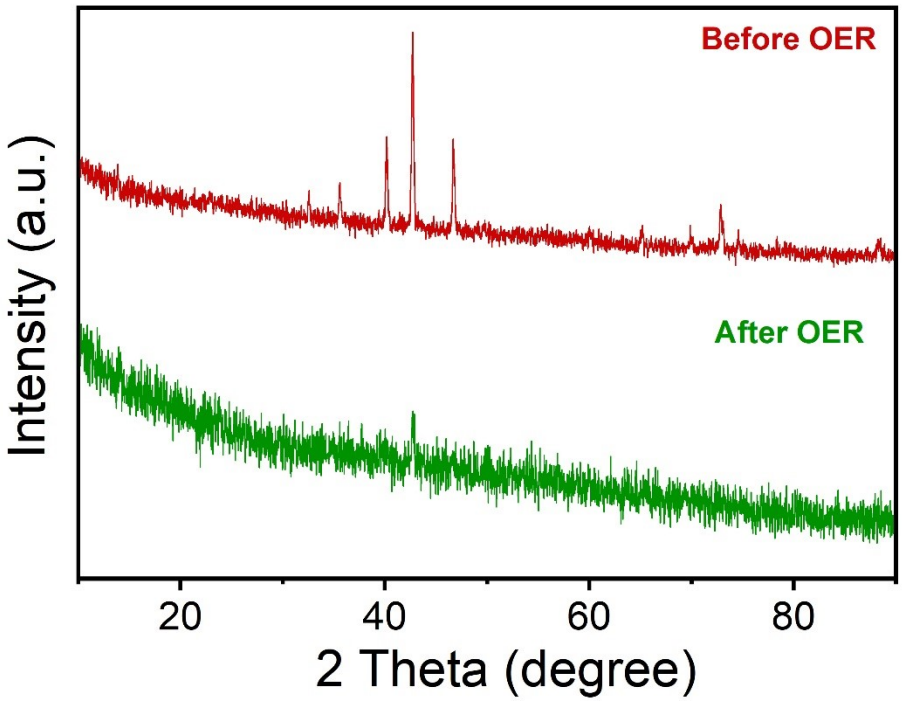

Figure S24. The XRD patterns of Co_6Mo_6C-Ir-2 NFs after OER stability test.

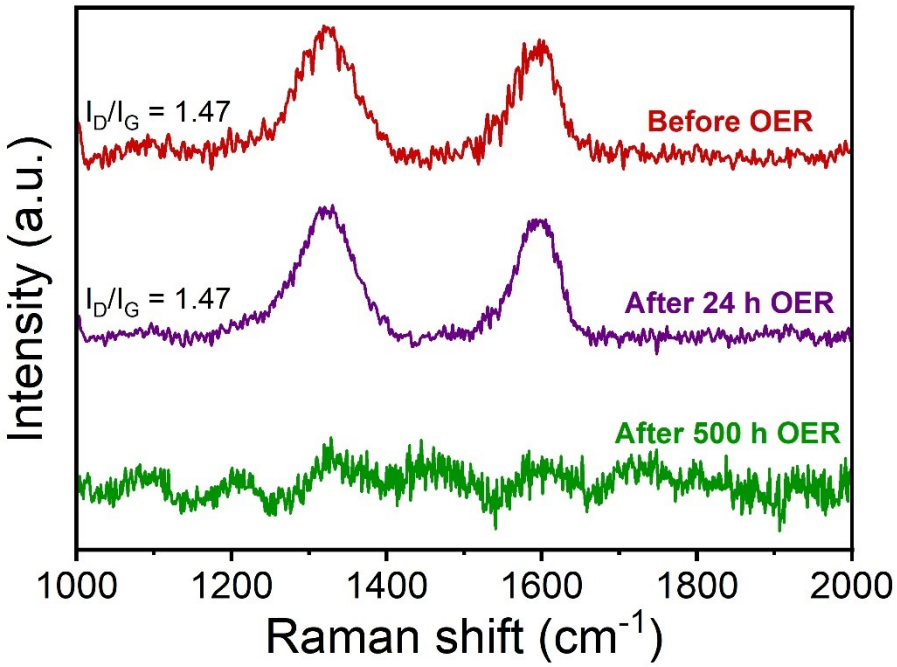

Figure S25. The Raman spectra of Co_6Mo_6C-Ir NFs before and after OER stability test.

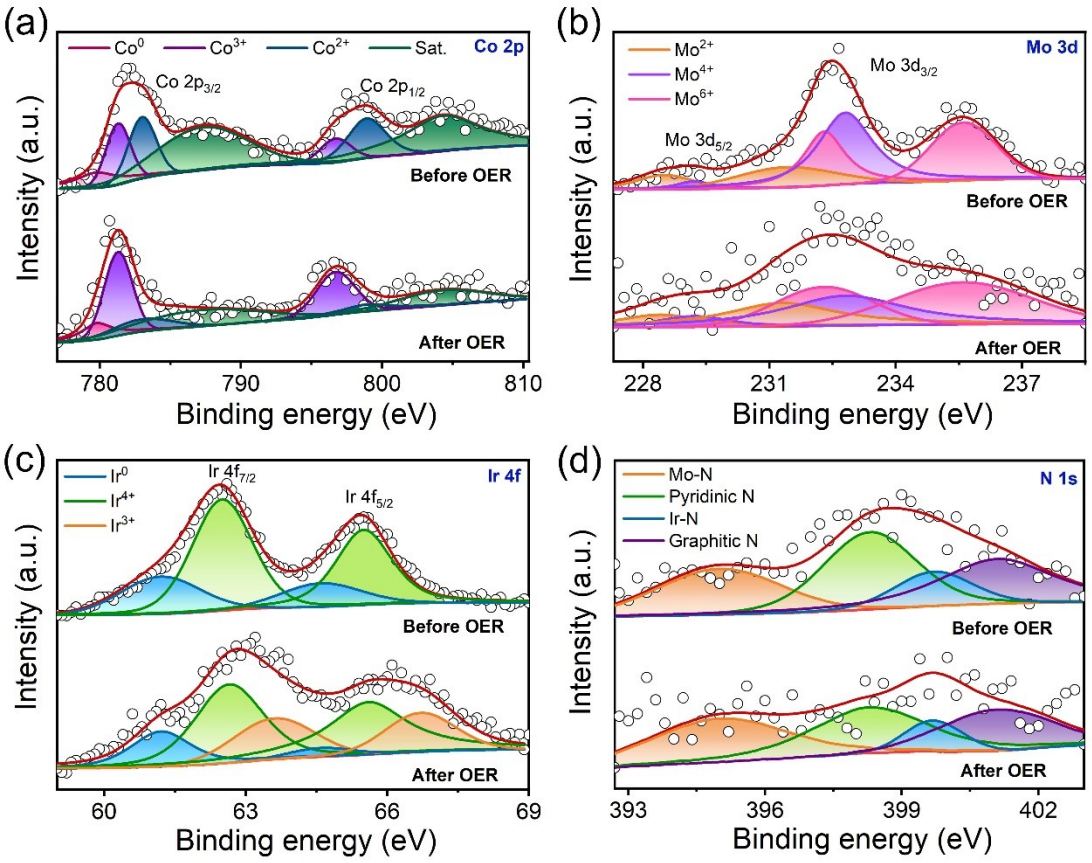

Figure S26. Typical high-resolution (a) Co 2p, (b) Mo 3d, (c) Ir 4f and (d) N 1s XPS spectra of Co_6Mo_6C-Ir-2 NFs before and after OER stability test.

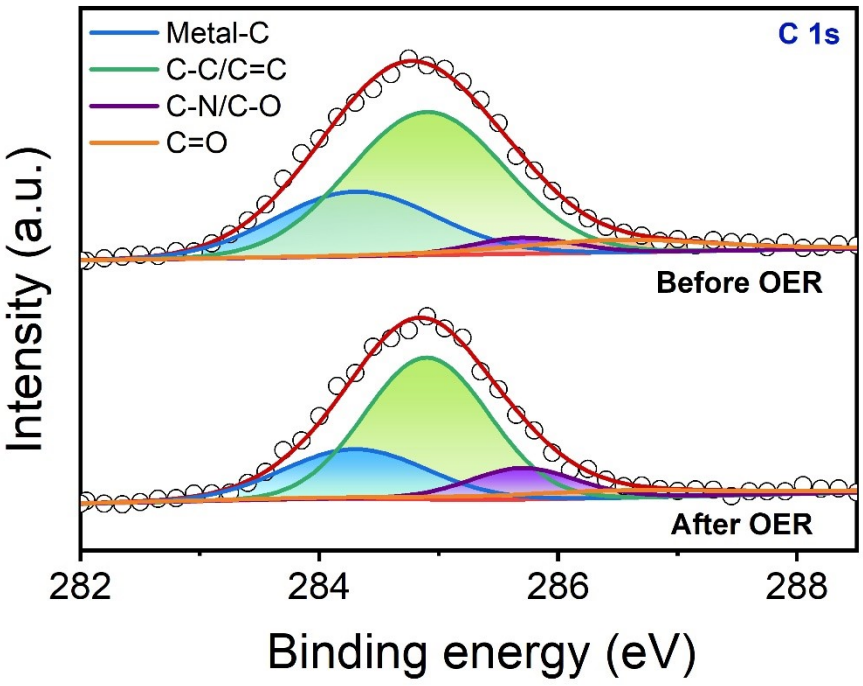

Figure S27. Typical high-resolution C 1s XPS spectra of Co_6Mo_6C-Ir-2 NFs before and after OER stability test.

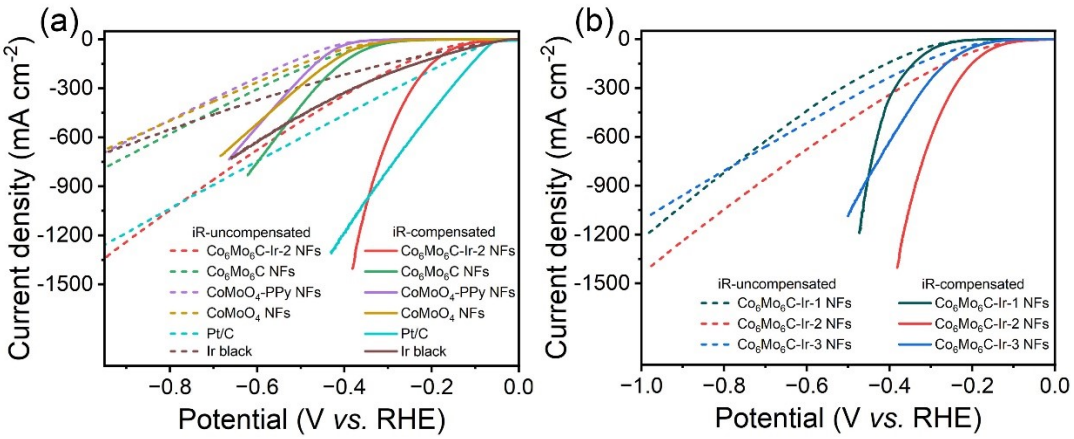

Figure S28. (a, b) The LSV curves of varied catalysts with and without iR compensation for HER.

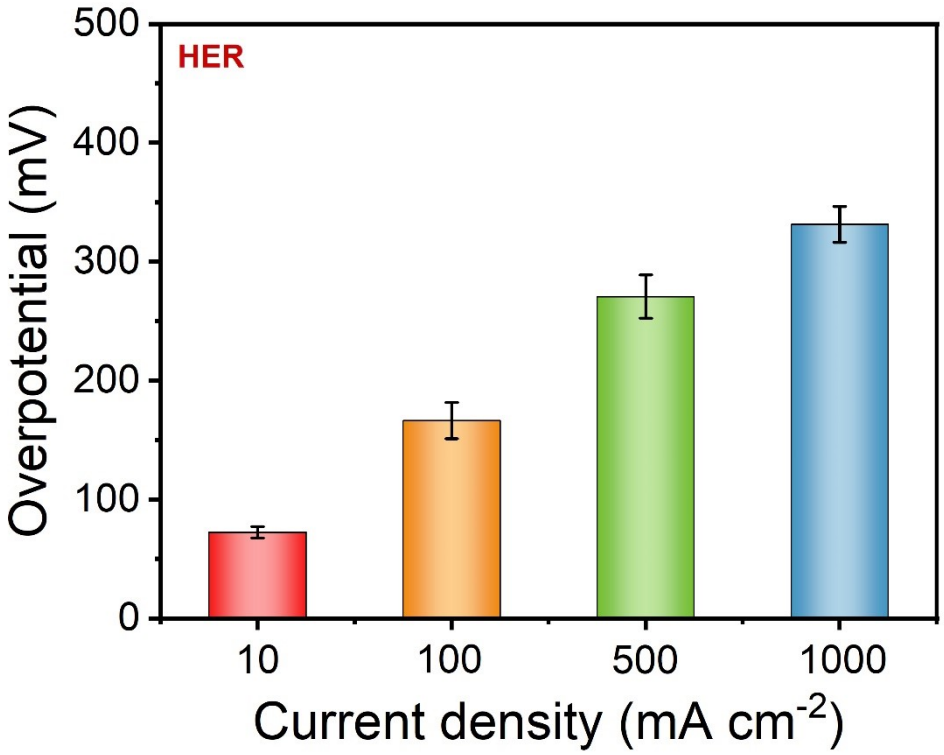

Figure S29. The evaluation of the HER overpotentials of Co_6Mo_6C-Ir NFs at 10, 100, 500 and 1000 mA cm^{-2}. Error bars represent the standard deviations of three independent measurements under the same conditions.

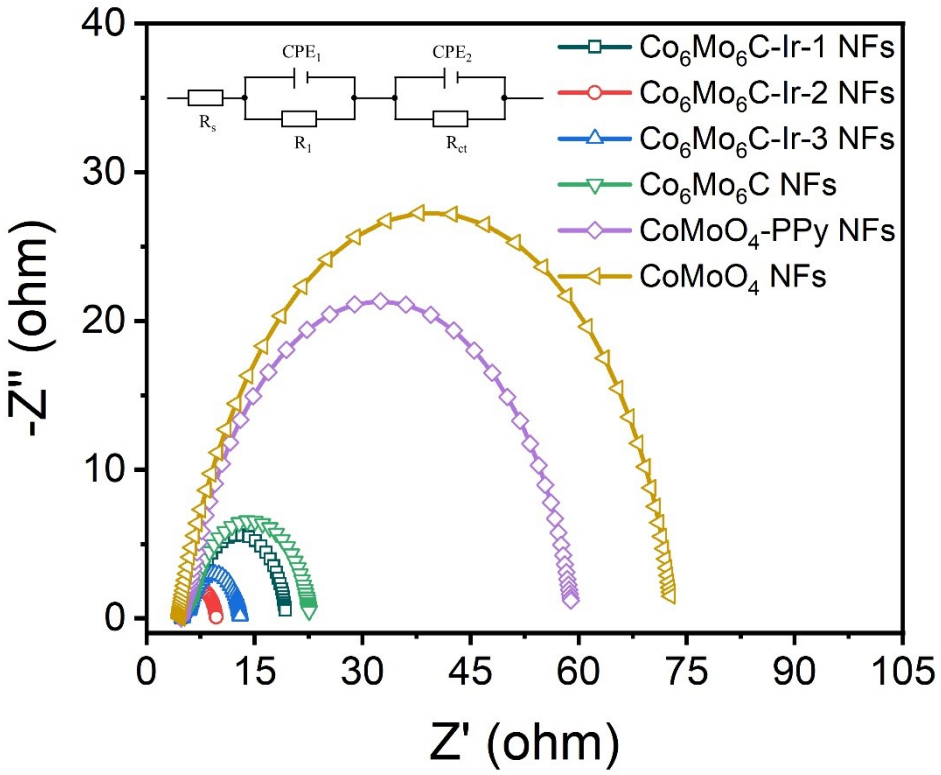

Figure S30. Nyquist plots of Co_6Mo_6C-Ir-2 NFs and other catalysts that performed at -1.2 V *vs.* Hg/HgO electrode.

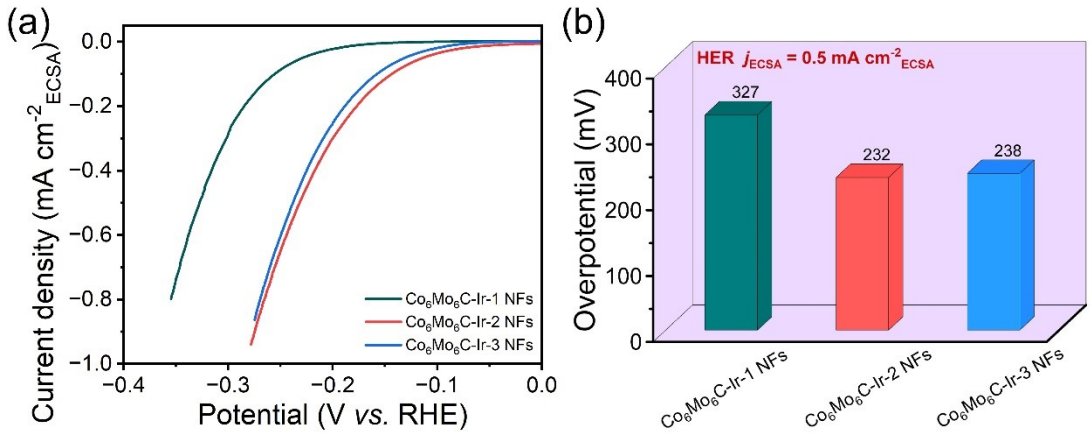

Figure S31. (a) HER polarization curves normalized to ECSA in 1 M KOH. (b) The corresponding specific activities at the current density of 0.5 mA cm^{-2}_{ECSA}.

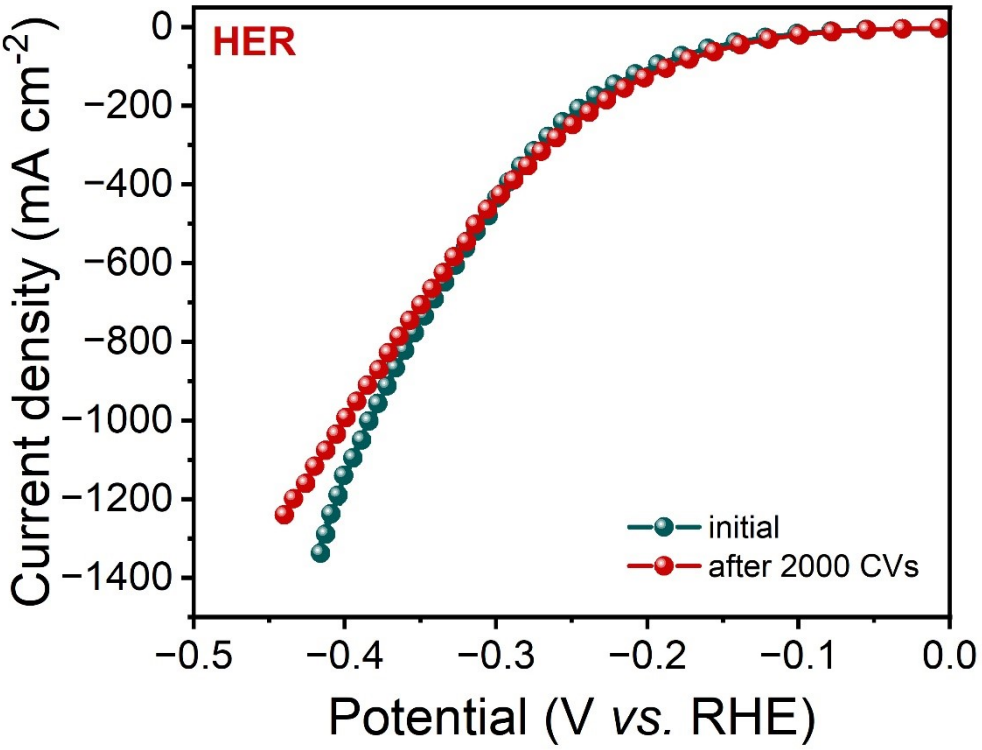

Figure S32. The LSV curves of Co_6Mo_6C-Ir-2 NFs for HER before and after 2000 CVs.

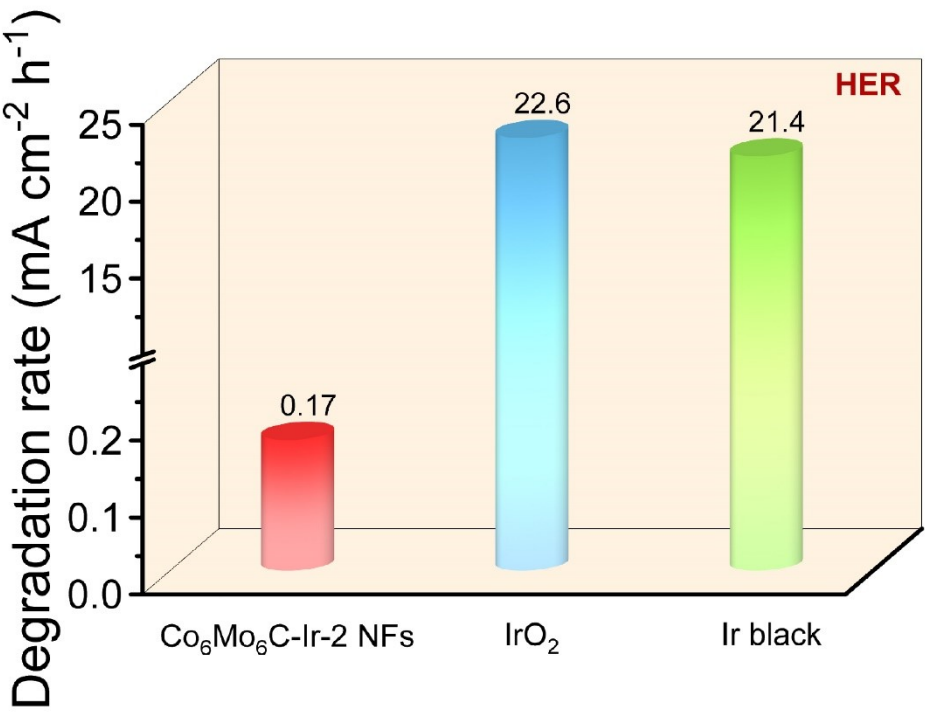

Figure S33. The degradation rates of catalysts for HER stability test.

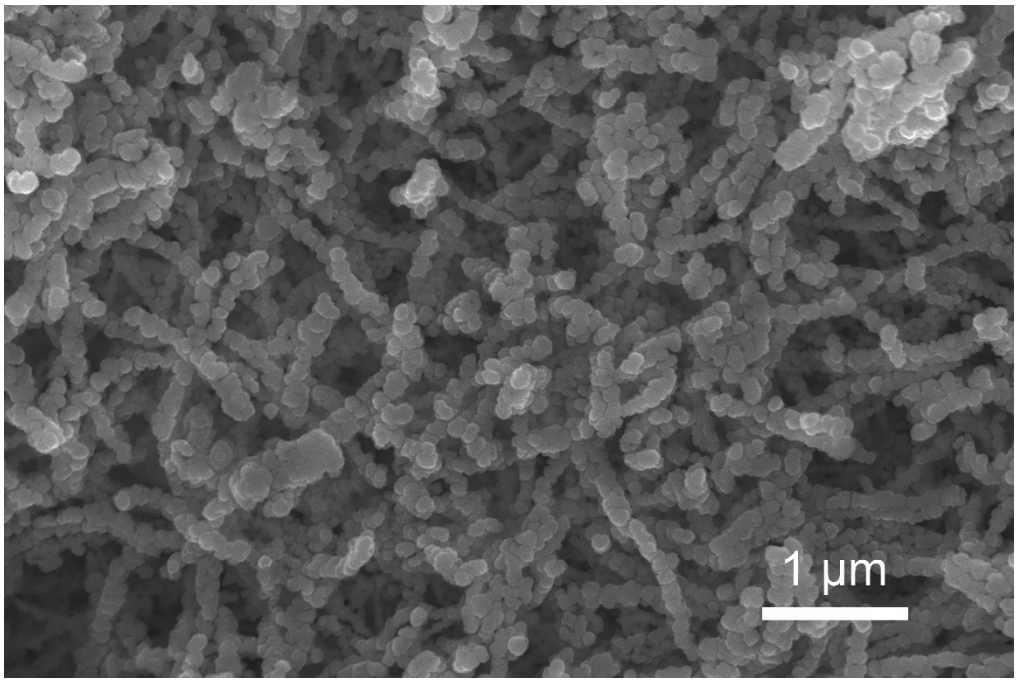

Figure S34. The SEM image of Co_6Mo_6C-Ir-2 NFs after HER stability test.

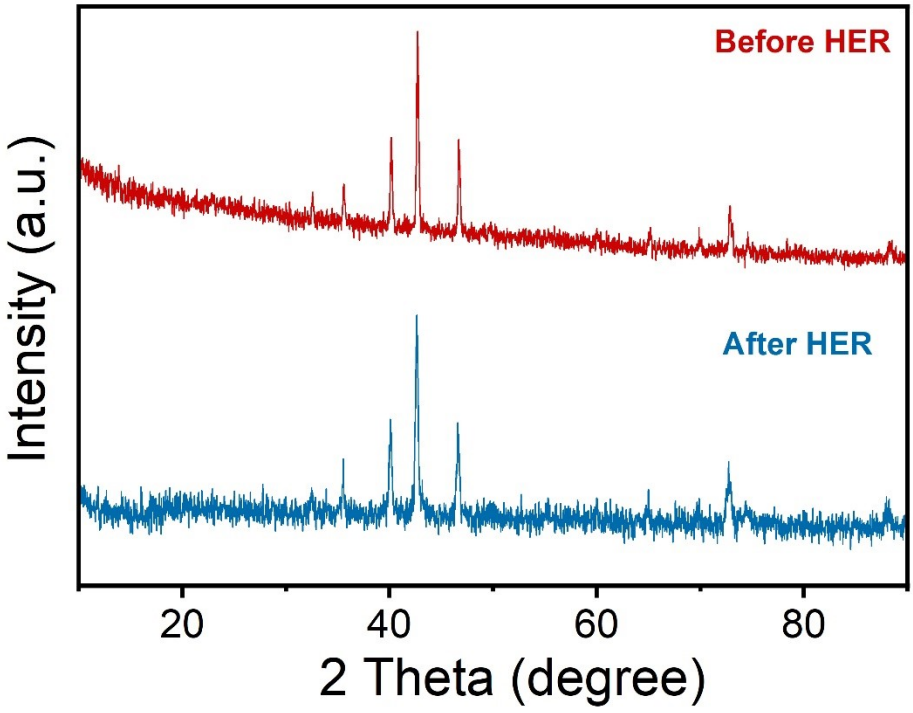

Figure S35. XRD patterns of Co_6Mo_6C-Ir-2 NFs after HER stability test.

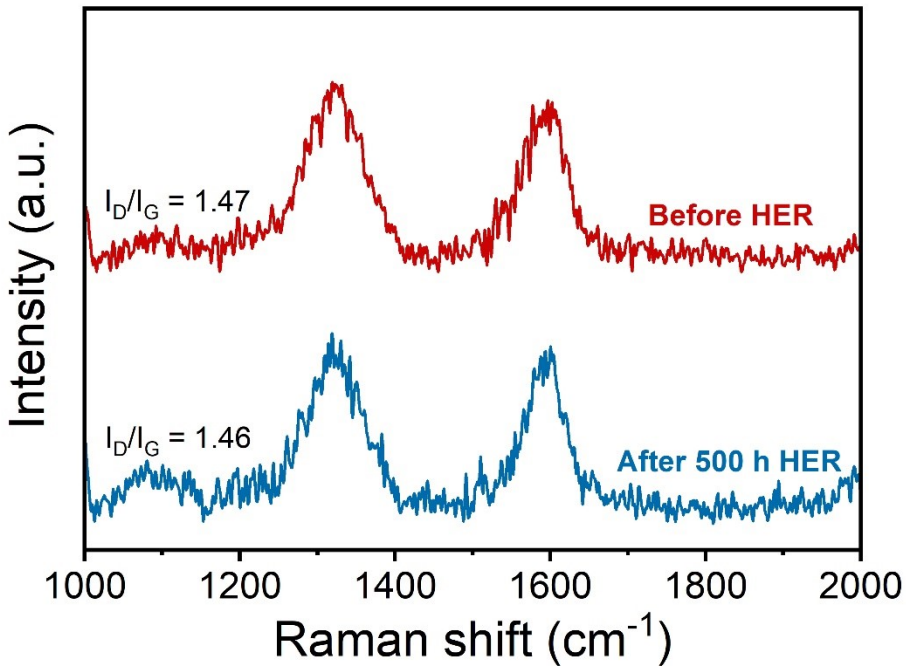

Figure S36. The Raman spectra of Co_6Mo_6C-Ir NFs before and after HER stability test.

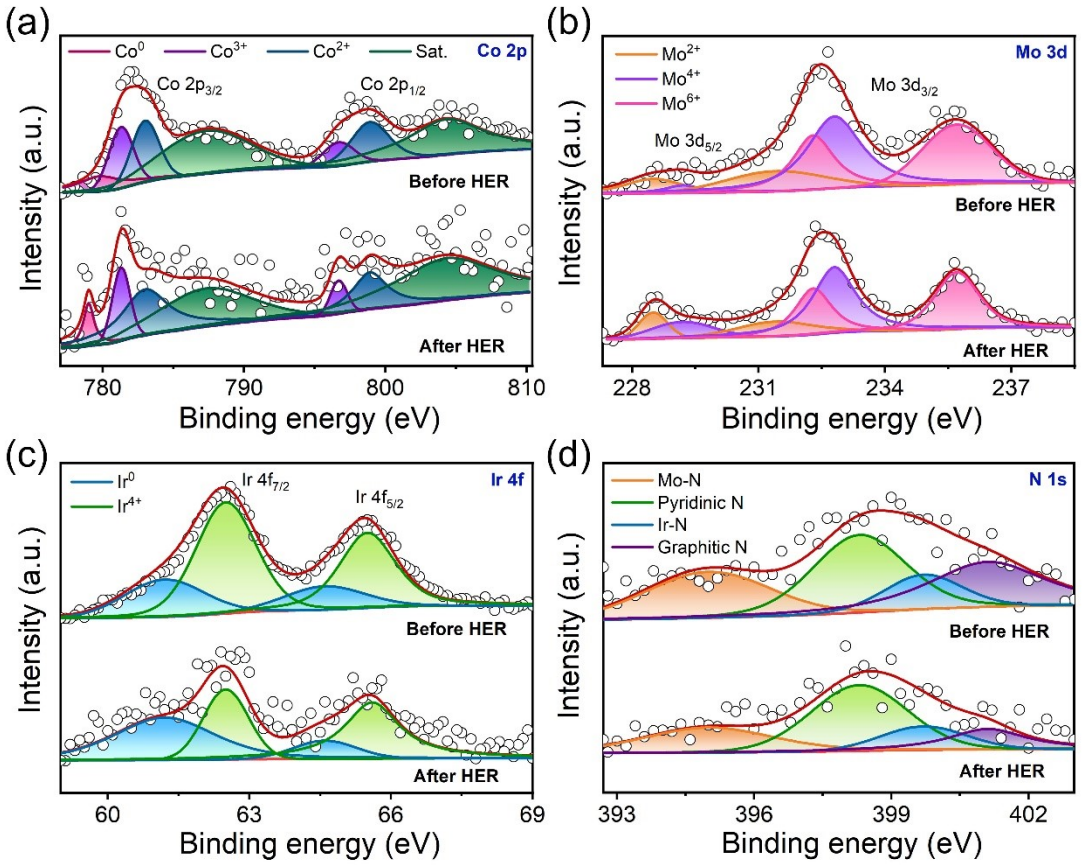

Figure S37. Typical high-resolution (a) Co 2p, (b) Mo 3d, (c) Ir 4f and (d) N 1s XPS spectra of Co_6Mo_6C-Ir-2 NFs before and after HER stability test.

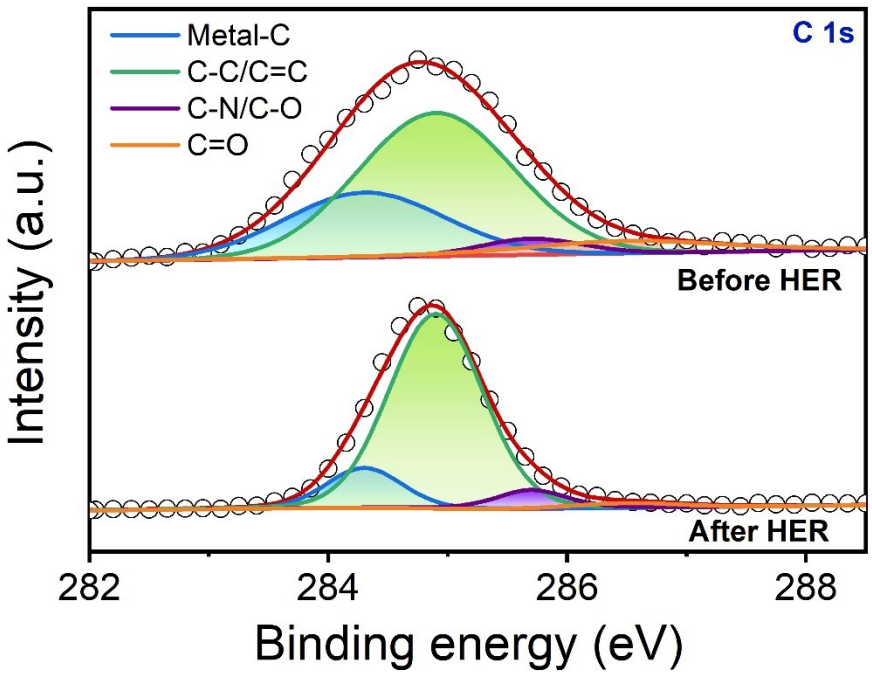

Figure S38. Typical high-resolution N 1s XPS spectra of Co_6Mo_6C-Ir-2 NFs before and after HER stability test.

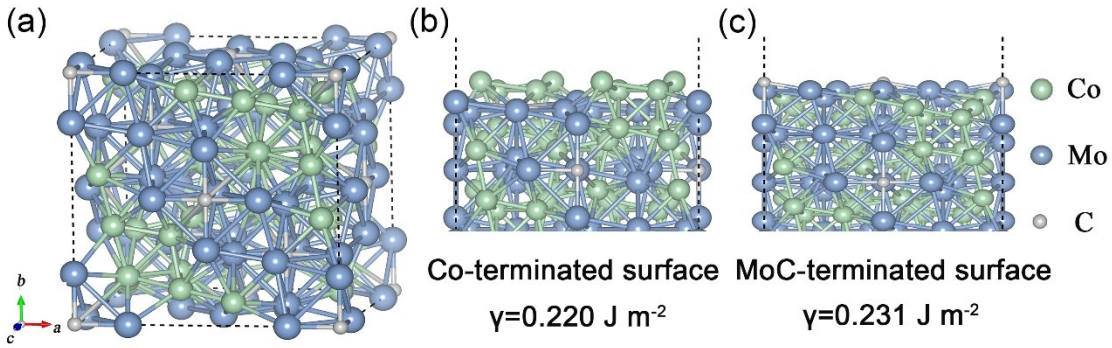

Figure S39. (a) The crystal structure of Co_6Mo_6C and (b, c) side view of possible exposed Co- or MoC-terminations for the low-index (100) facet, as well as the corresponding surface energies.

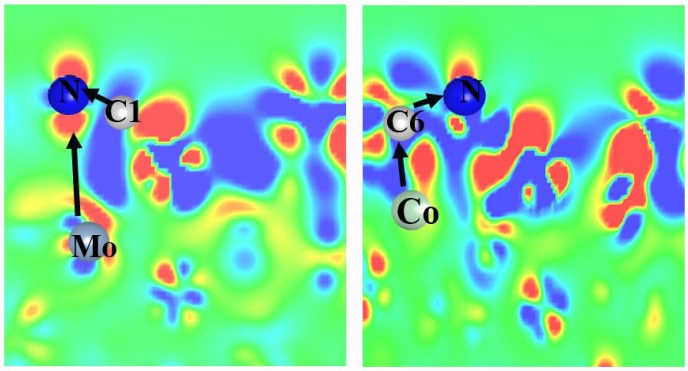

Figure S40. The charge density difference (Δρ) of Co_6Mo_6C-NF without Ir, in which the red and blue colors represent gaining and losing electrons, respectively, and the relevant electron transfer processes are also displayed.

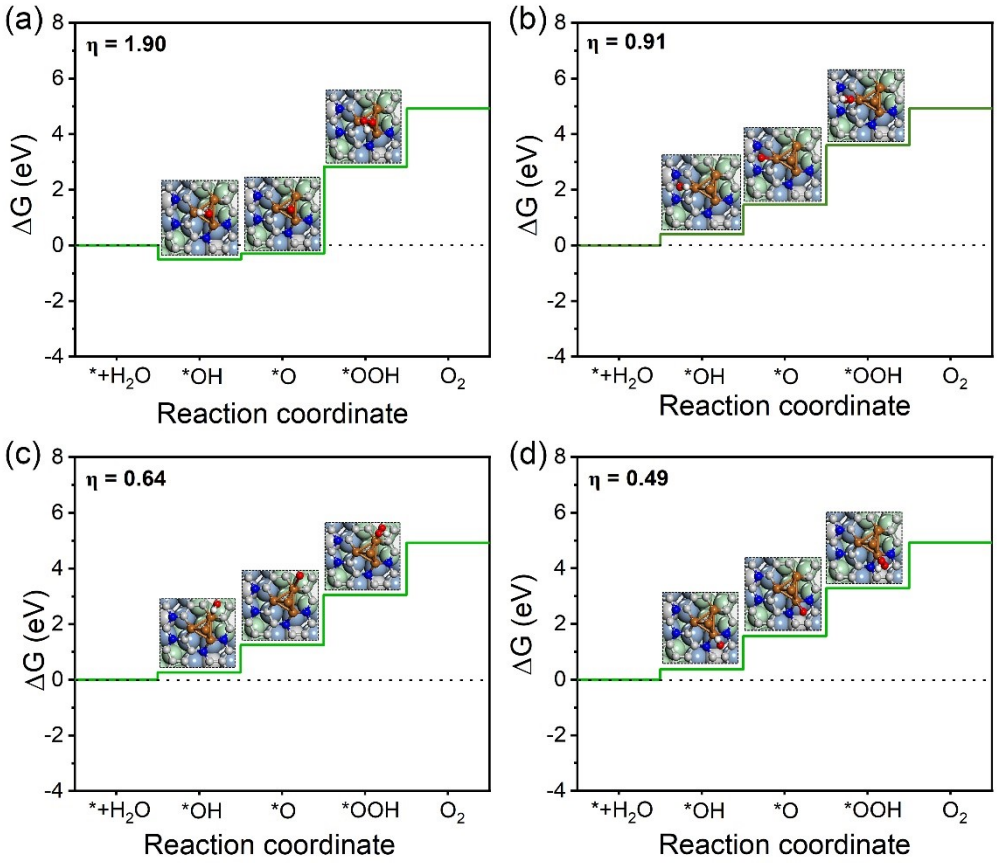

Figure S41. Free-energy diagrams for OER at the (a) T_{Ir1}, (b) T_{Ir2}, (c) T_{Ir3} and (d) T_{Ir4} sites.

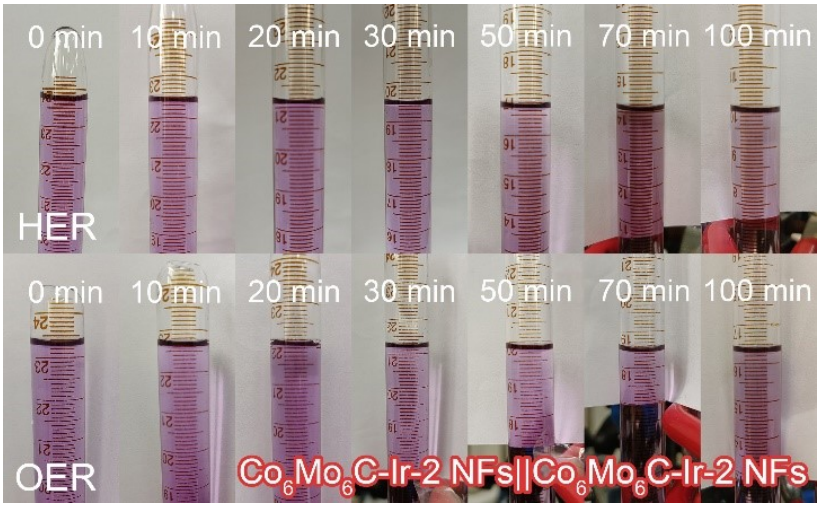

Figure S42. The photographs of H_2 and O_2 production of Co_6Mo_6C-Ir-2 NFs||Co_6Mo_6C-Ir-2 NFs electrolyzer.

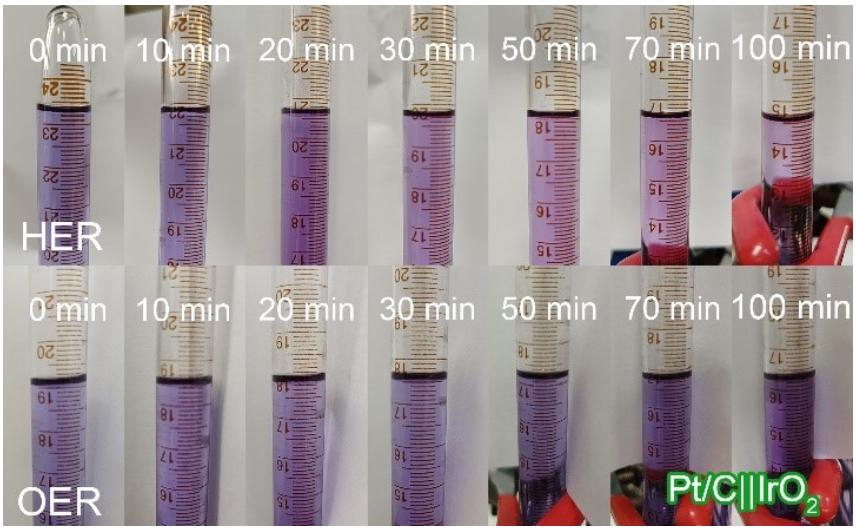

Figure S43. The photographs of H_2 and O_2 production of Pt/C||IrO_2 NFs electrolyzer.

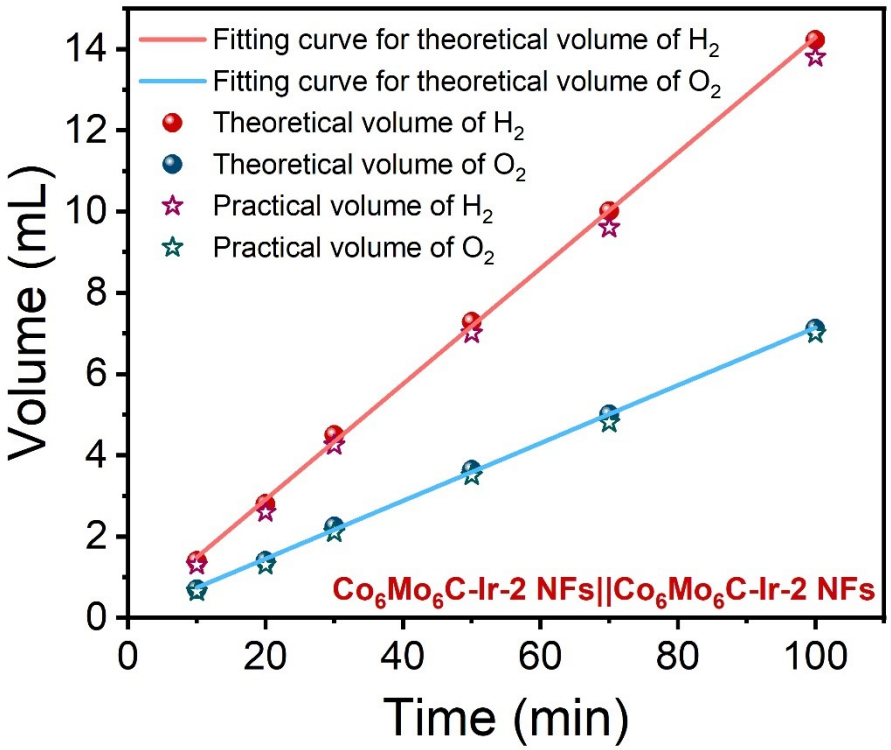

Figure S44. The comparison of theoretically calculated and experimentally measured evolved H_2 and O_2 gas for Co_6Mo_6C-Ir-2 NFs||Co_6Mo_6C-Ir-2 NFs electrolyzer.

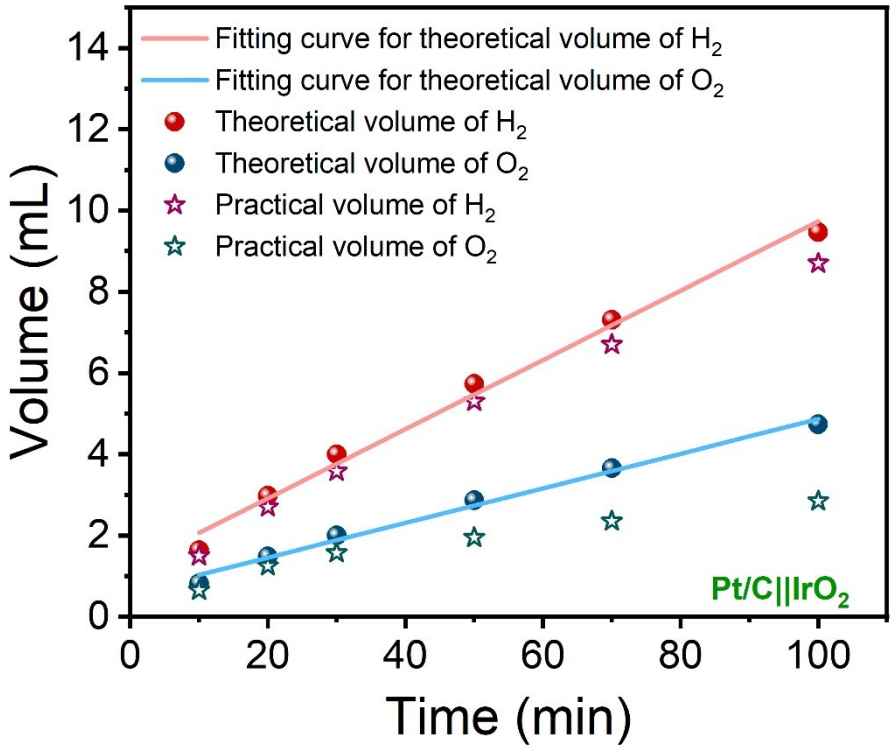

Figure S45. The comparison of theoretically calculated and experimentally measured evolved H_2 and O_2 gas for Pt/C||IrO_2 electrolyzer.

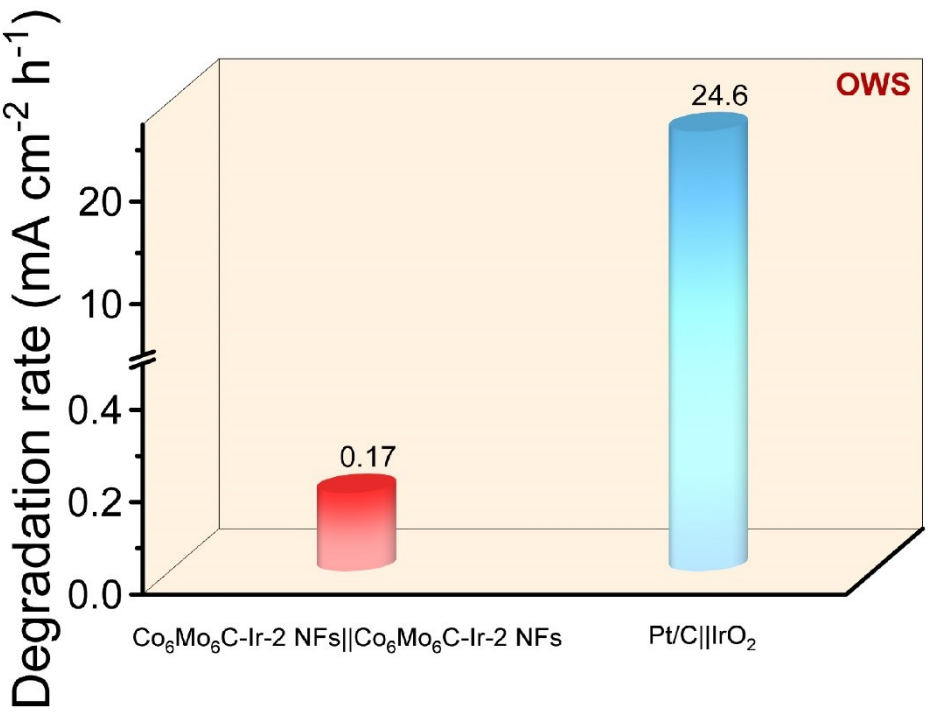

Figure S46. The degradation rates of electrolyzers for OWS stability test.

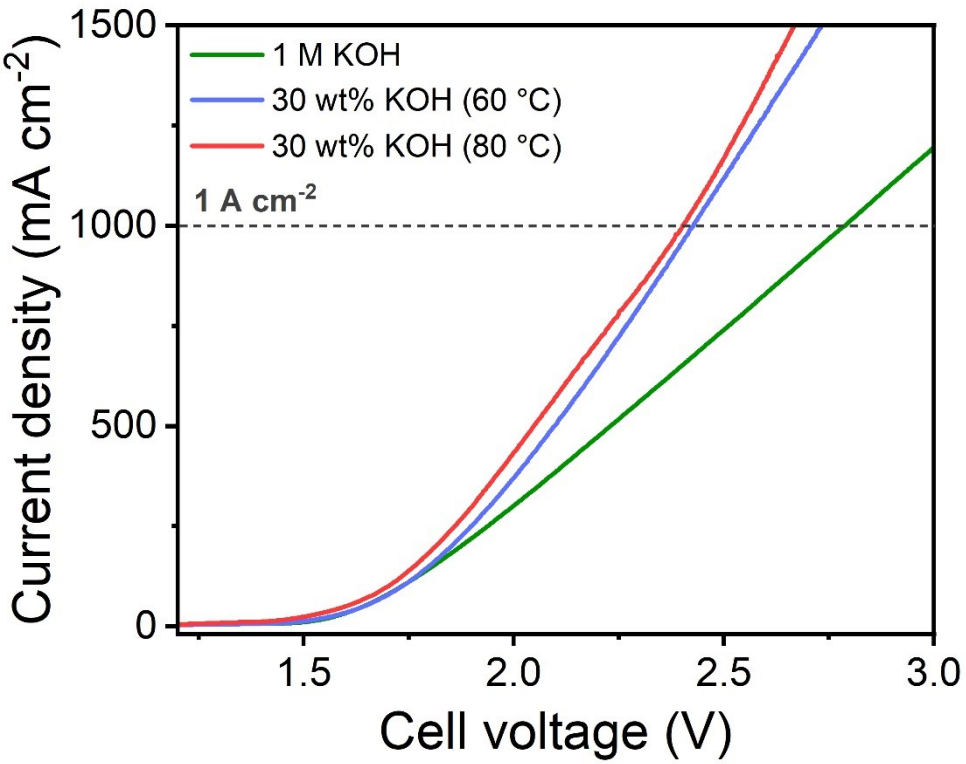

Figure S47. The polarization curves of Co_6Mo_6C-Ir-2 NFs in 1 M KOH, 30 wt% KOH (60 °C) and 30 wt% KOH (80 °C) for overall water splitting without iR compensation.

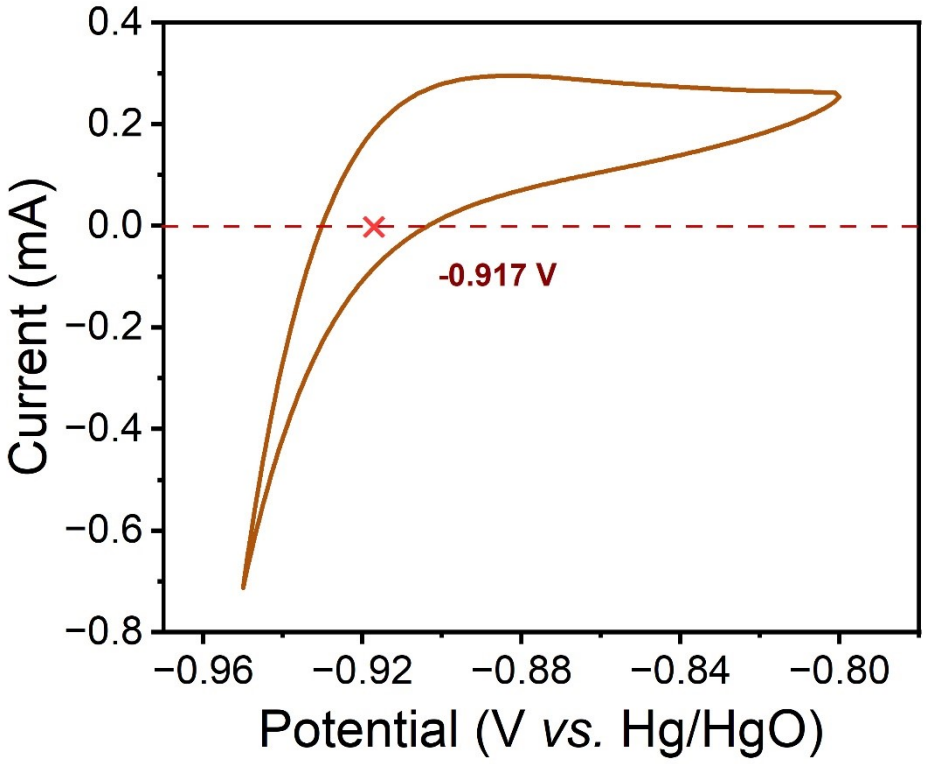

Figure S48. The CV curve for the calibration of the Hg/HgO reference electrode at the scan rate of 1 mV s^{-1} in H_2-saturated 1 M KOH solution.

Note: The calibration process of the Hg/HgO reference electrode: The H_2 was introduced into 1 M KOH electrolyte until it saturated. Then, two polished Pt plate electrodes and Hg/HgO electrode served as the working electrode, the counter electrode and the pre-calibrated reference electrode, respectively. Cyclic voltammetry (CV) at the scan rate of 1 mV s^{-1} was conducted to calibrate the reference potential of the Hg/HgO electrode in the high-purity H_2-saturated 1 M KOH electrolyte. According to the result of CV test, the thermodynamic potential (-0.917 V) was calculated. Hence, the Nernst equation in this work can be modified as follow: $E_{RHE} = E_{Hg/HgO} + 0.917$ V.

Table S1. The ICP results of prepared catalysts.

Catalysts	Co (wt %)	Mo (wt %)	Ir (wt %)
$CoMoO_4$ NFs	26.7	44.0	N/A
$CoMoO_4$-PPy NFs	13.3	25.8	N/A
Co_6Mo_6C NFs	33.8	64.4	N/A
Co_6Mo_6C-Ir-1 NFs	34.2	59.5	4.6
Co_6Mo_6C-Ir-2 NFs	33.7	58.7	5.9
Co_6Mo_6C-Ir-3 NFs	31.2	59.6	7.6

Table S2. Comparison of the OER activity of the Co_6Mo_6C-Ir-2 NFs catalyst with other reported non-noble catalysts in 1 M KOH solution.

Catalysts	J ($mA\ cm^{-2}$)	η (mV)	Tafel slope ($mV\ dec^{-1}$)	Reference
Co_6Mo_6C-Ir-2 NFs	10	209	46.8	This work
	100	257		
	500	297		
	1000	316		
Co_1Mn_1CH	100	387	N/A	J. Am. Chem. Soc. 2017, 139, 8320-8328.
	1000	46		
Co_2FeO_4	10	359	60	Nat. Commun. 2022, 13, 179.
CoFeZr oxides/NFs	20	264	54.2	Adv. Mater. 2019, 31, 1901439.
Ru-a-CoNi	100	285	66	Angew. Chem.-Int. Edit. 2022, 61, e202209075.
Fe-Mo-S/Ni_3S_2@NF	100	300	98	Chem. Eng. J. 2021, 404, 126483.
	500	367		
(NiCo)S1.33	10	302	N/A	Nat. Commun. 2023, 14, 1949.
RuO_2/CoO_x	10	240	70	Nat. Commun. 2022, 13, 5448.
CoO/hi-Mn_3O_4	10	378	61	Angew. Chem.-Int. Edit. 2017, 56, 8539-8543.
CoIr	10	235	70.2	Adv. Mater. 2018, 30, 1707522.
P-IrO_x@DG	10	248	52.8	Small 2021, 17, 2100121.
S/N-CMF@$Fe_xCo_yNi_{1-x-y}$-MOF	10	296	53.5	Adv. Mater. 2023, 10.1002/adma.202207888.
$NiCo_2S_4$@Mo-CoFe LDH/NF	500	295	83	Appl. Catal. B-Environ. 2022, 319, 121917.
	1000	332		
Ru−Co/ELCO	10	247	49.1	Angew. Chem.-Int. Edit. 2022, 61, e202205946.
CeO_2-$NiCoP_x$/NCF	500	455	72	Appl. Catal. B-Environ. 2022, 316, 121678.
N-Co_6Mo_6C NRs	10	310	59	J. Electroanal. Chem. 2020, 871, 114271.
$NiMoO_x$/NiMoS	1000	334	34	Nat. Commun. 2020, 11, 5462.
Ru-CoO_x/NF	1000	370	134	Small 2021, 17, 2102777.

Table S3. Comparisons of the C_{dl}, ECSA and RF values of Co_6Mo_6C-Ir-2 NFs with other catalysts.

Catalysts	C_{dl} (mF cm^{-2})	ECSA (cm^2)	RF
Co_6Mo_6C-Ir-1 NFs	9.3	20.93	232.5
Co_6Mo_6C-Ir-2 NFs	19.9	44.78	497.5
Co_6Mo_6C-Ir-3 NFs	8.3	18.68	207.5
Co_6Mo_6C NFs	1.1	2.48	27.5

Table S4. Comparison of the HER activity of the Co_6Mo_6C-Ir-2 NFs catalyst with other reported non-noble catalysts in 1 M KOH solution.

Catalysts	J ($mA\ cm^{-2}$)	η (mV)	Tafel slope ($mV\ dec^{-1}$)	Reference
Co_6Mo_6C-Ir-2 NFs	10	76	96.1	This work
	100	177		
	500	284		
	1000	348		
$CoSn_2$/NF	10	103	N/A	Angew. Chem.-Int. Edit. 2018, 57, 15237-15242.
Ni-Mo_xC/NC	10	162	104.8	ACS Appl. Mater. Interfaces 2018, 10, 35025-35038
Mo_2C-CoO@N-CNFs	10	115	76	Chem. Eng. J. 2023, 451, 139025.
FD-MoS_2-3	10	174	89	Nat. Commun. 2022, 13, 2193.
CoFeZr oxides/NFs	10	104	119.3	Adv. Mater. 2019, 31, 1901439.
HC-MoS_2/Mo_2C	1000	442	58	Nat. Commun. 2020, 11, 3724.
A-NiCo LDH/NF	100	151	57	Appl. Catal. B-Environ. 2020, 261, 118240
	1000	381		
S-$Co_{0.85}Se$-1	10	108	59	Angew. Chem.-Int. Edit. 2021, 60, 12360-12365.
NC/Ni_3Mo_3N/NF	1000	710*	42	Appl. Catal. B-Environ. 2020, 272, 118956.
Fe-Mo-S/Ni_3S_2@NF	100	266	123	Chem. Eng. J. 2021, 404, 126483.
	500	384		
N-MoO_2/Ni_3S_2 NF	1000	517	76	ACS Appl. Mater. Interfaces 2019, 11, 27743-27750.
S-$Co_{0.85}Se$-1	10	108	59	Angew. Chem.-Int. Edit. 2021, 60, 12360-12365.
IrFe/NC	1000	850	30	Appl. Catal. B-Environ. 2019, 258, 117965.
N-Co_6Mo_6C NRs	10	161	62	J. Electroanal. Chem. 2020, 871, 114271.
IrCu NWs	10	86	60	Chem. Eng. J. 2021, 416, 129128.
	100	180*		
Co-Mo_2C	10	92	89	Appl. Catal. B-Environ. 2021, 284, 119738.

* represents that the displayed value is estimated through the given figure from the literature.

Table S5. The structure parameters for the calculation model of composite Co_6Mo_6C-Ir system.

Lattice parameters

a	b	c	alpha	beta	gamma
21.44510	10.15250	30.00000	90.0000	90.0000	90.0000

Structure parameters

	Atom	x	y	z
1	Co	0.41773	0.83566	0.55557
2	Co	0.16586	0.16732	0.49577
3	Co	0.0421	0.91579	0.46409
4	Co	0.20869	0.41738	0.40133
5	Co	0.4579	0.08421	0.46409
6	Co	0.08254	0.33659	0.49434
7	Co	0.16864	0.33494	0.55877
8	Co	0.41677	0.66476	0.49457
9	Co	0.29211	0.41579	0.46409
10	Co	0.45869	0.91738	0.40133
11	Co	0.2079	0.58421	0.46409
12	Co	0.33356	0.83365	0.49644
13	Co	0.07656	0.18159	0.55796
14	Co	0.29131	0.58262	0.40133
15	Co	0.04131	0.08262	0.40133
16	Co	0.33897	0.66461	0.55702
17	Co	0.31291	0.62581	0.47914
18	Co	0.04988	0.42006	0.565
19	Co	0.19803	0.09785	0.56725
20	Co	0.0629	0.12581	0.47914
21	Co	0.29644	0.90852	0.5708
22	Co	0.45116	0.59538	0.56642

23	Co	0.1871	0.37419	0.47914
24	Co	0.4371	0.87419	0.47914
25	Co	0.92297	0.81565	0.55981
26	Co	0.66717	0.16283	0.49386
27	Co	0.54211	0.91579	0.46409
28	Co	0.70869	0.41738	0.40133
29	Co	0.9579	0.08421	0.46409
30	Co	0.58366	0.33401	0.49473
31	Co	0.66164	0.33087	0.5562
32	Co	0.91639	0.66335	0.49478
33	Co	0.79211	0.41579	0.46409
34	Co	0.95869	0.91738	0.40133
35	Co	0.7079	0.58421	0.46409
36	Co	0.83513	0.82948	0.49764
37	Co	0.58208	0.16371	0.5558
38	Co	0.79131	0.58262	0.40133
39	Co	0.54131	0.08262	0.40133
40	Co	0.83341	0.65629	0.56493
41	Co	0.81291	0.62581	0.47914
42	Co	0.55179	0.40804	0.56613
43	Co	0.70212	0.09765	0.56682
44	Co	0.56291	0.12581	0.47914
45	Co	0.80796	0.88544	0.57161
46	Co	0.94592	0.58101	0.56548
47	Co	0.6871	0.37419	0.47914
48	Co	0.9371	0.87419	0.47914
49	Mo	0.252	0.50298	0.53983
50	Mo	0.9987	0.50084	0.50104
51	Mo	0.39945	0.49911	0.43285

52	Mo	0.35056	0.00089	0.43285
53	Mo	0.24956	0.79889	0.43285
54	Mo	0.49956	0.29889	0.43285
55	Mo	0.22462	0.75427	0.52261
56	Mo	0.47392	0.25052	0.52203
57	Mo	0.375	0.25	0.45074
58	Mo	0.375	0.75	0.41388
59	Mo	0.12665	0.55129	0.52238
60	Mo	0.37621	0.4497	0.52268
61	Mo	0.125	0.75	0.45074
62	Mo	0.27488	0.24929	0.52332
63	Mo	0.12456	0.95281	0.52195
64	Mo	0.14945	0.99911	0.43285
65	Mo	0.25021	0.00162	0.50236
66	Mo	0.00044	0.70111	0.43285
67	Mo	0.99778	0.00199	0.5391
68	Mo	0.10055	0.50089	0.43285
69	Mo	0.125	0.25	0.41388
70	Mo	0.37314	0.04974	0.52199
71	Mo	0.02717	0.74555	0.52265
72	Mo	0.25045	0.20111	0.43285
73	Mo	0.75201	0.49708	0.55009
74	Mo	0.49954	0.49725	0.50141
75	Mo	0.89945	0.49911	0.43285
76	Mo	0.85056	0.00089	0.43285
77	Mo	0.74956	0.79889	0.43285
78	Mo	0.99956	0.29889	0.43285
79	Mo	0.72623	0.74513	0.5265
80	Mo	0.97202	0.25408	0.52329

81	Mo	0.875	0.25	0.45074
82	Mo	0.875	0.75	0.41388
83	Mo	0.62635	0.54832	0.52255
84	Mo	0.87024	0.44811	0.52386
85	Mo	0.625	0.75	0.45074
86	Mo	0.77394	0.24679	0.52157
87	Mo	0.62636	0.94798	0.52259
88	Mo	0.64945	0.99015	0.50312
90	Mo	0.50045	0.70111	0.43285
91	Mo	0.5001	0.99914	0.53927
92	Mo	0.60056	0.50089	0.43285
93	Mo	0.625	0.25	0.41388
94	Mo	0.87356	0.04601	0.52286
95	Mo	0.52662	0.74616	0.52084
96	Mo	0.75045	0.20111	0.43285
97	C	0.25	0	0.43163
98	C	0	0.5	0.43163
99	C	0.12615	0.75231	0.52635
100	C	0.37445	0.24957	0.5252
101	C	0.75	0	0.43163
102	C	0.5	0.5	0.43163
103	C	0.62644	0.74817	0.52584
104	C	0.87289	0.24735	0.52369
105	C	0.06844	0.99859	0.6263
106	C	0.1677	0.1226	0.63153
107	C	0.03488	0.1245	0.6192
108	C	0.13467	0.99767	0.63192
109	C	0.26709	0.99838	0.63134
110	C	0.36645	0.12639	0.62674

111	C	0.2344	0.12457	0.63093
112	C	0.33368	0.00025	0.6279
113	C	0.46553	0.00248	0.62005
114	C	0.56399	0.13023	0.62077
115	C	0.43233	0.12814	0.62368
116	C	0.53162	0.00274	0.61945
117	C	0.66349	0.00536	0.62433
118	C	0.76414	0.13209	0.62215
119	C	0.6306	0.13128	0.62173
120	C	0.72995	0.00947	0.62565
121	C	0.8637	0.00673	0.61966
122	C	0.96583	0.12819	0.61849
123	C	0.83197	0.13193	0.61878
124	C	0.93326	0.00462	0.61742
125	C	0.0679	0.24879	0.62431
126	C	0.16752	0.37455	0.62669
127	C	0.03521	0.37465	0.629
128	C	0.13515	0.2483	0.62617
129	C	0.26754	0.24903	0.62822
130	C	0.36584	0.37483	0.6279
131	C	0.23411	0.3737	0.62483
132	C	0.33327	0.2497	0.62808
133	C	0.4645	0.25324	0.62649
134	C	0.56505	0.3801	0.63045
135	C	0.43166	0.37555	0.62945
136	C	0.53162	0.25588	0.62479
137	C	0.66462	0.25893	0.62252
138	C	0.76532	0.377	0.61954
139	C	0.63189	0.38514	0.62313

140	C	0.73121	0.25395	0.62008
141	C	0.86452	0.25217	0.62149
142	C	0.96915	0.37606	0.62502
143	C	0.93295	0.25503	0.62059
144	C	0.06904	0.50063	0.62948
145	C	0.16713	0.62488	0.63201
146	C	0.03779	0.62707	0.62887
147	C	0.13518	0.50073	0.63011
148	C	0.2661	0.49944	0.62539
149	C	0.36531	0.6238	0.62568
150	C	0.23307	0.62434	0.63012
151	C	0.33261	0.49855	0.62582
152	C	0.46528	0.50181	0.62936
153	C	0.56732	0.63	0.62957
154	C	0.43268	0.62584	0.63032
155	C	0.53295	0.50412	0.62893
156	C	0.63252	0.63056	0.63043
157	C	0.73094	0.50193	0.62679
158	C	0.97246	0.6261	0.62578
159	C	0.83217	0.63358	0.62629
160	C	0.06888	0.75162	0.6288
161	C	0.16714	0.87304	0.63444
162	C	0.03653	0.87671	0.62336
163	C	0.1348	0.75027	0.6328
164	C	0.26569	0.74826	0.63139
165	C	0.36597	0.87474	0.62426
166	C	0.23375	0.87263	0.63392
167	C	0.33221	0.74807	0.62578
168	C	0.46635	0.74967	0.62475

169	C	0.56499	0.87676	0.62217
170	C	0.43304	0.87503	0.62074
171	C	0.53336	0.75242	0.62597
172	C	0.762	0.88701	0.63245
173	C	0.63049	0.87933	0.62351
174	C	0.7253	0.76929	0.64435
175	C	0.96896	0.8781	0.61779
176	C	0.82951	0.89585	0.63828
177	C	0.93852	0.75363	0.62698
178	N	0.83008	0.36388	0.62967
179	N	0.66447	0.50713	0.63128
180	N	0.93999	0.50139	0.62525
181	N	0.66376	0.75813	0.62986
182	Ir	0.8686	0.49695	0.66925
183	Ir	0.76571	0.62569	0.6726
184	Ir	0.87125	0.75492	0.67106
185	Ir	0.84185	0.60998	0.73833

Table S6. Comparison of the OWS activity of the Co_6Mo_6C-Ir-2 NFs catalyst with other reported non-noble catalysts in 1 M KOH solution.

Catalysts	J (mA cm^{-2})	Voltage (V)	Reference
Co_6Mo_6C-Ir-2 NFs	10	1.50	this work
	100	1.73	
	1000	2.79	
Ir_1@Co/NC	10	1.603	Angew. Chem.-Int. Edit. 2019, 58, 11868-11873.
Mo_2C-CoO@N-CNFs	10	1.56	Chem. Eng. J. 2023, 451, 139025.
MoP-Mo_2C/NPC	10	1.55	Chem. Eng. J. 2022, 431,133719.
	100	1.77	
$CoMnO_x$@CN	108	1.8	J. Am. Chem. Soc. 2015, 137, 14305-14312.
NiS_2/CoS_2	10	1.78	Adv. Mater. 2017, 29, 1704681.
CoFeZr oxides/NFs	10	1.63	Adv. Mater. 2019, 31, 1901439.
Ir-NR/C	10	1.57	Appl. Catal. B-Environ. 2020, 279, 119394.
N-Co_6Mo_6C NRs	10	1.58	J. Electroanal. Chem. 2020, 871, 114271.
IrW/C	10	1.55	ACS Central Sci. 2018, 4, 124-1252.
EG/$Co_{0.85}$Se/NiFe-LDH	10	1.67	Energy Environ. Sci. 2016, 9, 478-483.
$NiCo_2O_4$ microcuboids	10	1.65	Angew. Chem.-Int. Edit. 2016, 55, 6290-6294.
IrCu NWs	10	1.59	Chem. Eng. J. 2021, 416, 129128.
Co-Mo_2C	10	1.68	Appl. Catal. B-Environ. 2021, 284, 119738.
	100	1.95*	
Ir_{16}-PdCu/C	10	1.63	Nano Lett. 2021, 21, 5774-5781.
Co_4S_3/Mo_2C-NSC	10	1.62	Appl. Catal. B-Environ. 2020, 260, 118197.
RhCu NTs	10	1.59	Adv. Energy Mater. 2020, 10, 1903038.
$CoSn_2$/NF	10	1.55	Angew. Chem.-Int. Edit. 2018, 57, 15237-15242.

* represents that the displayed value is estimated through the given figure from the literature.

References

[1] G. Kresse and J. Hafner, *Phys. Rev. B*, 1993, **47**, 558.

[2] J. P. Perdew, K. Burke and M. Ernzerhof, *Phys. Rev. Lett.*, 1996, **77**, 3865.

[3] X. Wu, M. C. Vargas, S. Nayak, V. Lotrich and G. Scoles, *J. Chem. Phys.*, 2001, **115**, 8748.

[4] S. Grimme, *J. Comput. Chem.*, 2006, **27**, 1787.

[5] P. E. Blöchl, *Phys. Rev. B*, 1994, **50**, 17953.

[6] S. Haider, A. Roldan and N. H. de Leeuw, *J. Phys. Chem. C*, 2014, **118**, 1958.

[7] J. K. Norskov, T. Bligaard, A. Logadottir, J. R. Kitchin, J. G. Chen, S. Pandelov and J. K. Norskov, *J. Electrochem. Soc.*, 2005, **152**, J23.

[8] J. K. Norskov, J. Rossmeisl, A. Logadottir, L. Lindqvist, J. R. Kitchin, T. Bligaard and H. Jonsson, *J. Phys. Chem. B*, 2004, **108**, 17886.

[9] J. Rossmeisl, A. Logadottir and J. K. Norskov, *Chem. Phys.*, 2005, **319**, 178.

[10] A. Valdes, Z. W. Qu, G. J. Kroes, J. Rossmeisl and J. K. Norskov, *J. Phys. Chem. C*, 2008, **112**, 9872.